

Chandra & XMM-Newton Observations of NGC 5253. Analysis of the X-ray Emission from a Dwarf Starburst Galaxy.

Lesley K. Summers¹, Ian R. Stevens¹, David K. Strickland^{2*}
and Timothy M. Heckman²

¹ School of Physics & Astronomy, University of Birmingham, Edgbaston, Birmingham, B15 2TT, UK

lks@star.sr.bham.ac.uk; irs@star.sr.bham.ac.uk

² Department of Physics & Astronomy, The Johns Hopkins University, 3400 North Charles Street, Baltimore, MD 21218, USA

dks@pha.jhu.edu; heckman@pha.jhu.edu

Accepted; Received; in original form

ABSTRACT

We present *Chandra* and *XMM-Newton* X-ray data of NGC 5253, a local starbursting dwarf elliptical galaxy, in the early stages of a starburst episode. Contributions to the X-ray emission come from discrete point sources and extended diffuse emission, in the form of what appear to be multiple superbubbles, and smaller bubbles probably associated with individual star clusters. *Chandra* detects 17 sources within the optical extent of NGC 5253 down to a completeness level corresponding to a luminosity of 1.5×10^{37} erg s⁻¹. The slope of the point source X-ray luminosity function is -0.54 ± 0.21 , similar to that of other nearby dwarf starburst galaxies. Several different types of source are detected within the galaxy, including X-ray binaries and the emission associated with star-clusters.

Comparison of the diffuse X-ray emission with the observed H α emission shows similarities in their extent. The best spectral fit to the diffuse emission is obtained with an absorbed, two temperature model giving temperatures for the two gas components of ~ 0.24 keV and ~ 0.75 keV. The derived parameters of the diffuse X-ray emitting gas are as follows: a total mass of $\sim 1.4 \times 10^6 f^{1/2} M_\odot$, where f is the volume filling factor of the X-ray emitting gas, and a total thermal energy content for the hot X-ray emitting gas of $\sim 3.4 \times 10^{54} f^{1/2}$ erg. The pressure in the diffuse gas is $P/k \sim 10^6 f^{-1/2}$ K cm⁻³. We find that these values are broadly commensurate with the mass and energy injection from the starburst population. Analysis of the kinematics of the starburst region suggest that the stellar ejecta contained within it can escape the gravitational potential well of the galaxy, and pollute the surrounding IGM.

Key words: ISM: jets and outflows – galaxies: individual: NGC 5253 – galaxies: starburst – X-rays: galaxies.

1 INTRODUCTION

NGC 5253 is a starbursting dwarf elliptical galaxy which lies at a distance of ~ 3.15 Mpc (Freedman et al. 2001) and with an inclination of 67° (the mean value quoted by the Lyon/Meudon Extra-galactic Database [LEDA]). The signature of Wolf-Rayet stars have been detected in the nucleus of the galaxy (Schaerer et al. 1997, Walsh & Roy 1987) implying that this is a young starburst and as such allows an

opportunity for the study of the starburst phenomenon in its earlier stages of development and its effect on galaxy evolution in the local Universe. In fact, Rieke, Lebofsky & Walker (1988) went so far as to classify it as one of the youngest starbursts known. Dwarf galaxies, as the basic building blocks in the hierarchical merging cosmology scenario, are likely to have harboured the earliest sites of star-formation in the Universe and so their study in the local Universe can give insight into the evolution of such objects at high redshift. Observations of local edge-on starburst galaxies (Strickland et al. 2000; Weaver 2001) are presenting a picture of kpc-scale,

* *Chandra* Fellow

soft X-ray emitting, bipolar outflows in the form of galactic winds transporting mass, newly synthesised heavy elements and energy into the intergalactic medium (IGM). A similar outflow is seen in the dwarf starburst galaxy NGC1569 (Martin, Kobulnicky & Heckman 2002), while the dwarf NGC 4449 shows what may be the beginnings of a galactic wind emerging from an extended superbubble (Summers et al. 2003). The same situation seems to be the case in the NGC 3077 dwarf (Ott, Martin & Walter 2003). These winds result from the pressure driven outflows along these galaxy's minor axis produced from the efficient thermalization of the mechanical energy from the supernovae (SN) explosions and stellar winds of the massive stars in their OB associations and super star-clusters (SSC). NGC 5253 being both inclined to our line-of-sight and young presents a less clearly observable picture. Its youth means that it is unlikely to have developed a superwind and the diffuse X-ray emission observed is much more likely to be associated with multiple superbubbles around its OB associations and SSC, as suggested from earlier *ROSAT* observations of this galaxy (Strickland & Stevens 1999).

Observations of NGC 5253 at radio wavelengths have shown it to have a very flat centimetre-wavelength continuum which is indicative of thermal emission from HII regions, with only low levels of synchrotron emission from supernova remnants (Beck et al. 1996; Turner, Ho & Beck 1998). Ferrarese et al. (2000) quote a low metallicity of $0.2Z_{\odot}$, based on the work of Webster & Smith (1983). This figure suggests that a large amount of metal enrichment has not occurred in the central HII regions, and may be further evidence of the youth of the starburst region. The total and HI masses for the galaxy are calculated to be $6.4 \times 10^8 M_{\odot}$ and $8.3 \times 10^7 M_{\odot}$ from 21 cm observations (Reif et al. 1982), corrected for the difference in assumed distance to NGC 5253. Later VLA 21 cm observations show NGC 5253 to be peculiar, in so much as its neutral hydrogen appears to rotate about the optical major axis of the galaxy (Kobulnicky & Skillman 1995). However, CO observations (Turner, Beck & Hurt 1997; Meier, Turner & Beck 2002) detect sources which are coincident with the dust lane seen to the SE of the nucleus of the galaxy in optical images, and these CO clouds appear to be infalling into NGC 5253. Consequently, the dynamical situation in NGC 5253, rotation or infall, is not completely clear.

Infrared emission is detected from what seems to be a highly obscured, massive ($10^5 - 10^6$ stars), small (\sim a few pc diameter) and very young globular cluster in the central starburst region of the galaxy (Gorjian, Turner & Beck 2001). This source contributes $\sim 50\%$ of the total observed infrared luminosity of the galaxy. A summary of some of the properties of NGC 5253 is given in Table 1, along with estimates of the current star-formation rate of the galaxy estimated from far-infrared and H α fluxes.

Caldwell & Phillips (1989), using broadband multi-colour (UBV) CCD images, narrow-band H α and long-slit CaII triplet spectra, determined that NGC 5253 had undergone an increased rate of star-formation throughout the galaxy about $10^8 - 10^9$ yr ago, as suggested by the presence of over 100 star clusters of a similar age lying outside the nuclear region. They also established that the intense star-formation now occurring in the nuclear region of the galaxy began around 10 Myr ago, giving an upper limit for the age

of superbubbles associated with it. More recently, Tremonti et al. (2001) analysed several clusters in NGC 5253, determining ages in the range of 1 to 8 Myr. Calzetti et al. (1997) also noted two other clusters with older ages, determined to be between 10 and 50 Myr.

The two very bright SN explosions seen in this galaxy in 1895 and 1972 are amongst the apparently brightest recorded extra-galactic SNe (Ardeberg & de Groot 1973) and may be associated with the large scale star-formation, although neither was particularly centrally located. The Fabry-Perot H α images of Marlowe et al. (1995) show that the ionized gas in the galaxy has a complex distribution, consisting of a bright central region extending $\sim 30''$ from the centre in a N-S direction, embedded within a system of loops and filaments, with an overall extent of $\sim 2'$. To the NW and WSW of the centre are 2 large superbubbles with diameters $\sim 1'$, expanding at $\sim 35 \text{ km s}^{-1}$, while to the east side of the galaxy, a pair of radially oriented filaments are detected. This latter observation is suggestive of the rupture of a superbubble blown by the stellar activity in the central regions.

NGC 5253 has previously been observed at X-ray wavelengths with the *Einstein* IPC (Fabbiano, Kim & Trinchieri 1992) and both the *ROSAT* PSPC (Martin & Kennicutt 1995; Stevens & Strickland 1998) and HRI (Strickland & Stevens 1999). The *Einstein* IPC and *ROSAT* PSPC results showed soft thermal X-ray emission from what appeared to be an extended source, suggestive of a luminous superbubble. The better spatial resolution of the *ROSAT* HRI instrument detected a complex of at least five X-ray sources, that could be young superbubbles blown by individual young star clusters in the starburst region. The total X-ray luminosity determined from these observations was similar and lies in the range of $(2.4 - 4.1) \times 10^{38} \text{ erg s}^{-1}$, depending on the value adopted for the absorbing column density.

In Section 2 we describe the *Chandra* and *XMM-Newton* observations. The X-ray emission from the whole galaxy, the point sources and the diffuse emission are discussed in Section 3. Section 4 contains a more general discussion of the morphology of the X-ray emission and its relationship to emission from other wavebands, along with a determination of the dynamics of the expanding superbubbles of the central region and their effect on NGC 5253. Our main conclusions are summarised in Section 5.

2 OBSERVATIONS AND ANALYSIS

A 57 ks *Chandra* observation of NGC 5253 was obtained on Jan 13th – 14th 2001 and a 46 ks *XMM-Newton* observation was obtained on 8th – 9th August of the same year. For the *Chandra* data, analysis was carried out on the data contained within the S3 chip of the ACIS-S instrument using *CIAO* (version 2.2.1), *HEASOFT* (version 5.1), *XSPEC* (version 11.1.0) and *ASTERIX* (version 2.3-b1). The data were first reprocessed using *CALDB* version 2.9 and then filtered to remove periods of flaring and lower than average count rates using the *lc_clean.sl* script with a 5σ clipping, leaving a total of 47.8 ks of useful data. The data were then further filtered to retain only data in the energy band from 0.3 – 8.0 keV and were background subtracted using the appropriately scaled *Chandra* X-ray Observatory Center

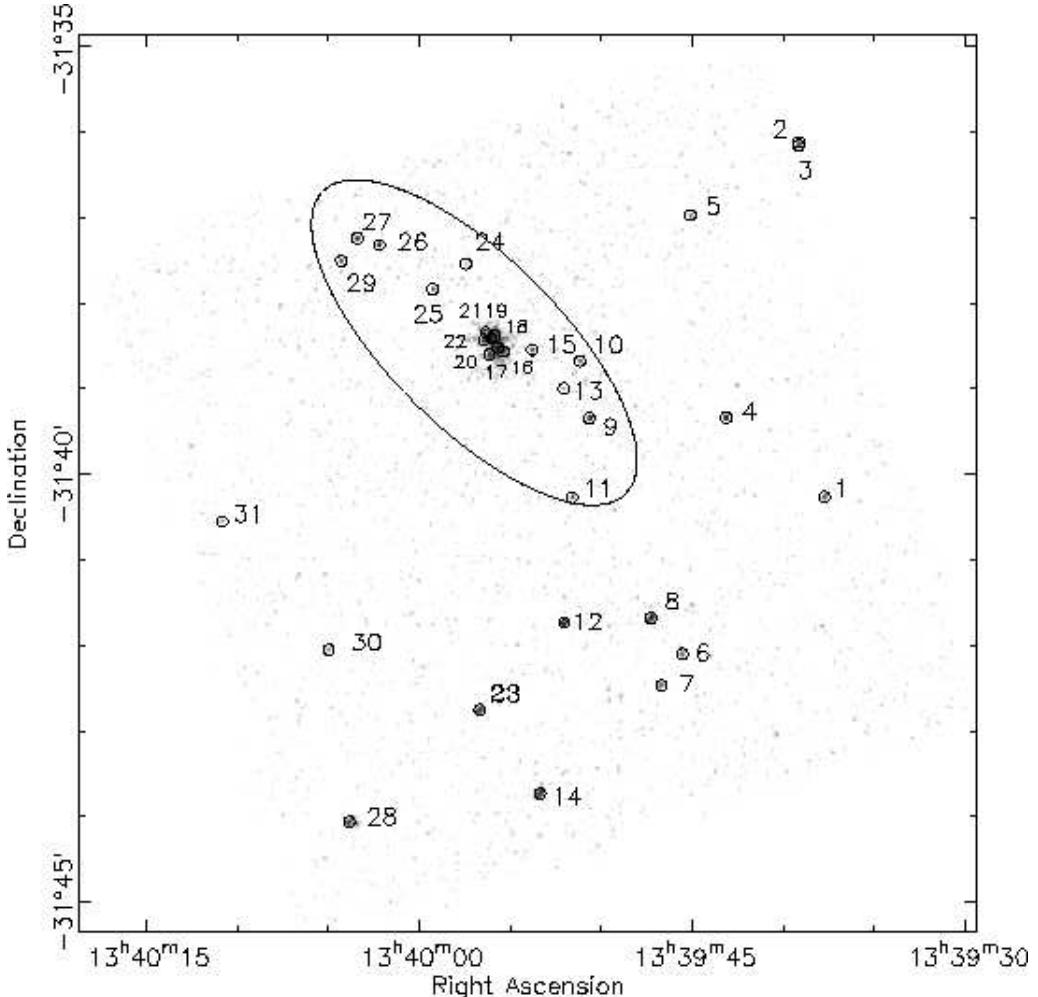


Figure 1. Low resolution (smoothed using a Gaussian with FWHM of 4 pixels $\sim 2''$), background subtracted *Chandra* image, in the 0.3 – 8.0 keV energy band, showing the full ACIS-S3 chip field of view, marked with the 31 point sources (Table 2). The image is an inverted log greyscale with the flux density ranging from 7.63×10^{-14} erg s $^{-1}$ cm $^{-2}$ arcmin $^{-2}$ to 9.72×10^{-11} erg s $^{-1}$ cm $^{-2}$ arcmin $^{-2}$. The D_{25} ellipse is also shown. North is to the top and East is to the left.

(CXC) background event data set. After production of an exposure map, the point sources present in the data were detected using the *CIAO wavdetect* tool, run with an exposure map and a source significance threshold of 9.5×10^{-7} , a value of $\sim (\text{number of pixels})^{-1}$ which should have limited the number of false detections to ~ 1 . A total of 31 point sources were detected and these are shown in Fig. 1, overlaid on a smoothed image of the ACIS-S3 chip (smoothed with a Gaussian having a FWHM of 4 pixels $\sim 2''$), while their positions and background subtracted count rates are listed in Table 2. Of these 31 sources, 17 lie within the optical extent of the galaxy, as shown by the D_{25} ellipse (de Vaucouleurs et al. 1991) on Fig. 1. These 17 sources are the ones most likely to be associated with NGC 5253 and so are the only ones considered further in this analysis. We note that results from this data have already been presented as part of a survey of the point source populations of nearby galaxies by Colbert et al. (2004), and a comparison with these results will be presented later.

From the *XMM-Newton* observation, only the European Photon Imaging Camera (EPIC) data has been analysed. Removal of flares using a recursive 3σ clipping technique

and standard pattern and flag filtering for the three cameras left 39.0 ks of useful data for MOS1, 39.6 ks for MOS2 and 26.7 ks for PN. These data were then also filtered to retain only data in the 0.3 – 8.0 keV energy band in line with the *Chandra* data. A background subtracted (using the David Lumb ‘blank sky’ and Philippe Marty ‘closed’ events files) mosaic of the exposure corrected images from the three cameras is shown in Fig. 2. The (0,0) point on this image lies at the centre of the D_{25} ellipse at a position of $\alpha = 13^h 39^m 56.2^s$, $\delta = -31^\circ 38' 29.9''$. The diffuse X-ray emission is seen to be extended to the WSW of the nucleus which is not apparent in the *Chandra* image. The latter does however show evidence of absorption of the X-ray emission due to the presence of the dust lane that extends E from the nuclear region, which is not apparent on the *XMM-Newton* data. It is also apparent from comparing Figs. 1 and 2 that some of the sources within the *Chandra* ACIS-S3 field-of-view are exhibiting variability. In the eight months between the two observations, sources 25 and 30 have faded whilst six possible additional sources are apparent in the *XMM-Newton* data, to the east of source 1, south-east of source 7, north-east of source 12, north of source 24, north of source

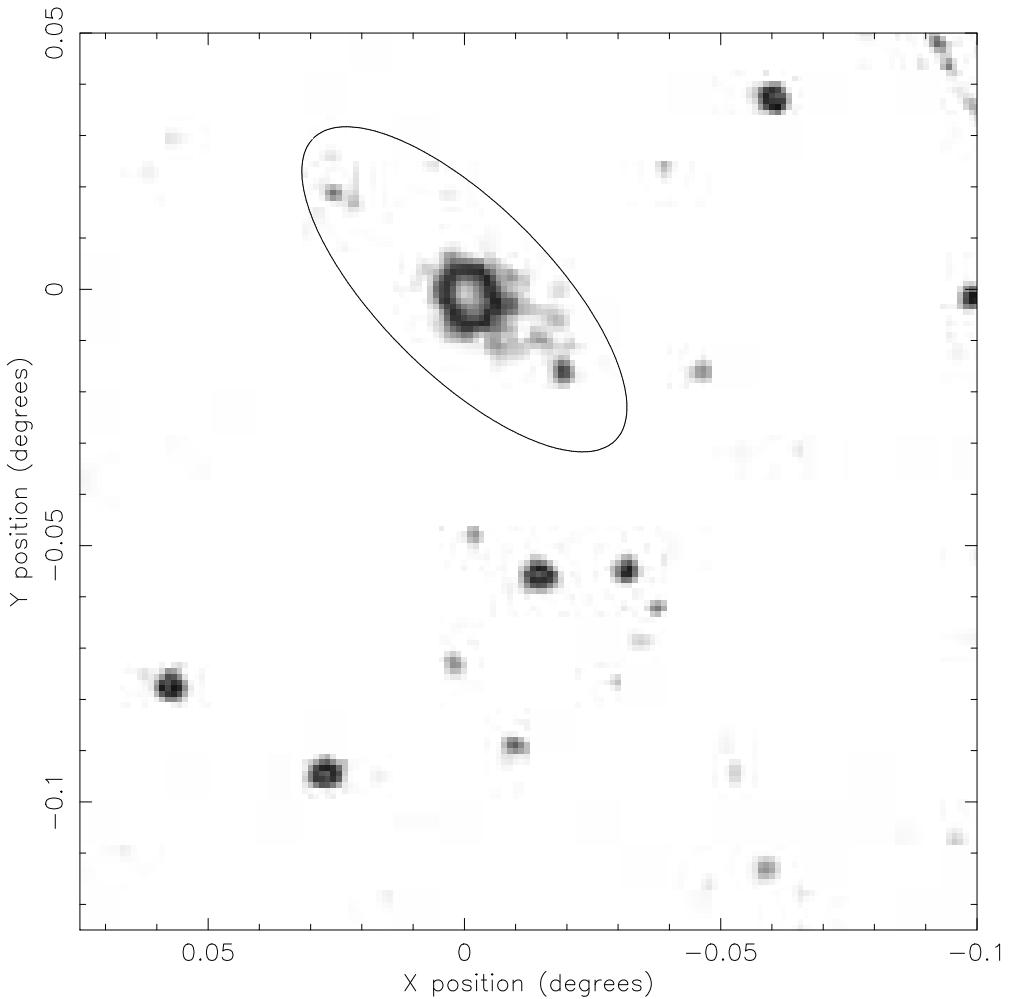


Figure 2. Low resolution (smoothed using a Gaussian with FWHM of 2 pixels $\sim 8''$), *XMM-Newton*, background subtracted and exposure corrected, mosaiced image of the data from the EPIC MOS1, MOS2 and PN cameras, in the $0.3 - 8.0$ keV energy band. The image is an inverted log greyscale with the flux density ranging from 5.2×10^{-14} erg s $^{-1}$ cm $^{-2}$ arcmin $^{-2}$ to 2.1×10^{-12} erg s $^{-1}$ cm $^{-2}$ arcmin $^{-2}$, with North to the top and East to the left. The D_{25} ellipse is also shown. The X-ray emission is extended towards the WSW.

26 and north of source 27. The last three in this list may be associated with NGC 5253 as they lie just inside the D_{25} ellipse. Fig. 3 shows the position and extent of the *Chandra* sources overlaid on the unsmoothed *XMM-Newton* mosaic and shows that a large fraction of what appears to be extended diffuse emission to the SW along the galaxy's major axis is more likely to be associated with point sources. However the diffuse emission does show extension to both the NW and SE along the minor axis, which may be associated with the shells and radial filaments seen in H α images (Marlowe et al. 1995).

After detection, the point sources were subtracted from the *Chandra* data so that the diffuse X-ray emission contained within that observation could be investigated. Also, a 3 colour adaptively smoothed image of the central region of the galaxy has been produced using *csmooth* in fft (fast Fourier transform) mode and this is shown in Fig. 4. The lower and upper sigmas for deriving the smoothing kernel were set at 2 and 5 respectively. This image shows that the spectral characteristics of the sources vary and that the diffuse emission appears to consist mainly of soft emission lying behind regions of varying absorption. The red, green and blue

images used correspond to energy bands of $0.3 - 1.1$ keV, $1.1 - 3.8$ keV and $3.8 - 8.0$ keV respectively. These bands were chosen so that the total number of counts in each band was approximately equal and thereby maximising the S/N ratio for the bands. The diffuse emission is seen to be confined predominantly to the nuclear region of the galaxy and the position of the indentation seen to the East, suggesting heavy absorption, corresponds to the position of the dust lane identified in the galaxy (Hunter 1982). In addition the effect of the dust is seen, in the reduction of intensity and change of colour as a result of the absorption of the softer emission, in the darker band running from E to W across the nuclear region.

3 RESULTS

3.1 Integrated Emission

The background subtracted spectrum of the total X-ray emission from within the D_{25} ellipse of NGC 5253 was fitted separately for the four instruments (ACIS-S, MOS1, MOS2 and PN), using the modified Levenberg-Marquardt method

Table 1. Details of NGC 5253. The distance is from Freedman et al. (2001), other data is from the LEDA and NED databases. The infrared luminosity L_{IR} is calculated using the 12, 25, 60 and 100 μ m IRAS fluxes (Sanders & Mirabel 1996) and the H α luminosity is from Marlowe et al. (1997, corrected for distance). The corresponding star-formation rates (SFR) for both the IR and H α luminosities are calculated using the conversion formulae in Kennicutt (1998).

Parameter	Value
Classification	Im pec, HII
Distance	3.15 Mpc
RA (J2000)	12 39 56.0
Dec (J2000)	-31 38 36
D_{25} ellipse	4.8' \times 1.9'
Position angle	45°
m_B	10.75
$B - V$	0.43
L_{IR}	4.5×10^{42} erg s $^{-1}$
$L_{H\alpha}$	2.6×10^{40} erg s $^{-1}$
SFR rate (IR)	0.2 M $_{\odot}$ yr $^{-1}$
SFR rate (H α)	0.2 M $_{\odot}$ yr $^{-1}$

Table 2. Positions and count rates of the 31 sources detected in the NGC 5253 *Chandra* S3 chip data. Column 1 is the source number ordered in increasing R.A.. Columns 2 and 3 give the R.A. and Dec. of each source and Column 4 lists their background subtracted count rates.

Source	RA (h m s)	Dec (° ' '')	Count Rate ($\times 10^{-3}$ cts s $^{-1}$)
1	13 39 37.73	-31 40 15.8	0.77 ± 0.15
2	13 39 39.16	-31 36 06.9	0.32 ± 0.09
3	13 39 39.17	-31 36 09.2	0.42 ± 0.10
4	13 39 43.15	-31 39 20.2	1.07 ± 0.16
5	13 39 45.12	-31 36 58.2	0.37 ± 0.10
6	13 39 45.53	-31 42 06.1	0.39 ± 0.10
7	13 39 46.69	-31 42 28.0	0.43 ± 0.11
8	13 39 47.27	-31 41 40.7	1.95 ± 0.22
9	13 39 50.66	-31 39 20.7	1.50 ± 0.18
10	13 39 51.17	-31 38 40.8	0.32 ± 0.09
11	13 39 51.62	-31 40 16.2	0.48 ± 0.11
12	13 39 51.96	-31 41 43.9	4.03 ± 0.30
13	13 39 52.07	-31 38 59.7	0.19 ± 0.07
14	13 39 53.36	-31 43 43.9	1.42 ± 0.20
15	13 39 53.80	-31 38 32.7	0.66 ± 0.13
16	13 39 55.39	-31 38 32.8	0.80 ± 0.17
17	13 39 55.69	-31 38 31.5	1.02 ± 0.20
18	13 39 55.85	-31 38 22.8	1.03 ± 0.20
19	13 39 56.04	-31 38 24.8	1.43 ± 0.23
20	13 39 56.15	-31 38 35.9	0.58 ± 0.16
21	13 39 56.35	-31 38 20.5	8.22 ± 0.43
22	13 39 56.45	-31 38 25.8	1.53 ± 0.21
23	13 39 56.67	-31 42 45.3	1.57 ± 0.21
24	13 39 57.43	-31 37 32.5	1.50 ± 0.06
25	13 39 59.27	-31 37 50.2	0.33 ± 0.09
26	13 40 02.19	-31 37 19.1	0.96 ± 0.15
27	13 40 03.40	-31 37 14.5	0.78 ± 0.13
28	13 40 03.84	-31 44 03.7	1.25 ± 0.21
29	13 40 04.29	-31 37 30.3	0.41 ± 0.10
30	13 40 04.97	-31 42 03.0	0.24 ± 0.08
31	13 40 10.81	-31 40 33.2	0.29 ± 0.09

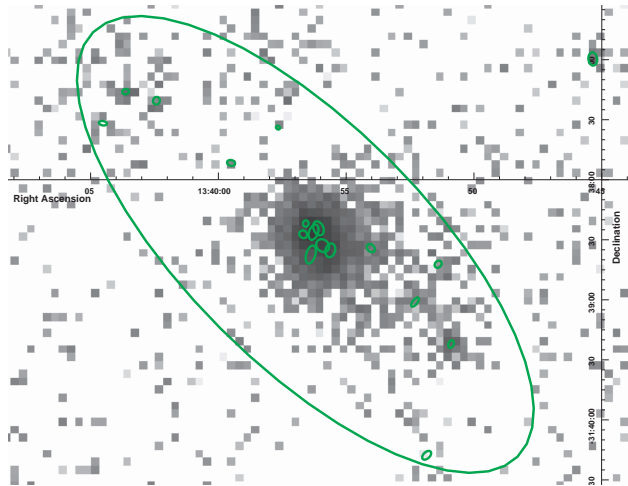


Figure 3. Unsmoothed background subtracted and exposure corrected, mosaiced image of the data from the *XMM-Newton* EPIC MOS1, MOS2 and PN cameras in the 0.3 – 8.0 keV energy range. The overlaid small ellipses show the positions and sizes of the sources detected in the *Chandra* data. The D_{25} ellipse is also shown. The extension in the X-ray emission towards the WSW is largely associated with point sources, but the emission is also slightly extended to the NW and SE along the galaxy's minor axis, as well as along the major axis. North is to the top and East is to the left.

and standard χ^2 statistic from *XSPEC*, with an absorbed 2 thermal component plus power-law fit, the same model that was fitted in earlier work to the similar dwarf starburst galaxy NGC 4449 (Summers et al. 2003). It was found though, for NGC 5253 that each component had to be fitted with a separate absorbing column, in addition to the absorption due to the interstellar medium within the Milky Way (Galactic column density, $N_{H(GAL)} = 3.87 \times 10^{20}$ cm $^{-2}$), to obtain a satisfactory fit. Another difference in the fitting for these two galaxies was in the energy range over which the spectral fitting was carried out. The NGC 5253 *Chandra* data was found to contain both a hard excess above ~ 6.0 keV and a soft excess below ~ 0.37 keV, neither of which could be adequately dealt with by either the flare removal or background subtraction. Even the use of a local background instead of the background event data set did not remove them and so the spectral fitting for all the instruments was confined to the 0.37 – 6.0 keV energy band for ease of comparison of the results from the two different telescopes. In addition, a single simultaneous fit to the data from the three *XMM-Newton* cameras was performed. The two absorbed thermal components were modelled using the *wabs* (photo-electric absorption using Wisconsin cross-sections) and *mekal* thermal plasma codes within *XSPEC*. Initially, Galactic absorption was assumed for all the column densities and a value of 0.19 Z_{\odot} assumed for the metallicity of the X-ray emitting gas (Ferrarese et al. 2000). The results are summarised in Table 3 and the fitted spectra for the *Chandra* data and simultaneous fit to the *XMM-Newton* data are shown in Fig. 5. Two thermal plasmas were used to represent the diffuse emission firstly because multi-phase models are seen to be needed to best fit the emission from other starburst galaxies (e.g. NGC 253, Strickland et

al. 2002; NGC 1569, Martin et al. 2002; NGC 4449, Summers et al. 2003), and secondly because single temperature fits to just the diffuse emission do not have a wide enough energy distribution to fit the spread seen in the data and so are statistically less robust.

We note that the MOS1 data gives substantially different results from the other two *XMM-Newton* cameras, particularly for the column densities and metallicities. There is also a difference between the results obtained from the two satellites, with the *Chandra* data giving higher column densities for the soft thermal and for the power-law components. The average unabsorbed flux, in the 0.37 – 6.0 keV energy band, from NGC 5253 for the *Chandra* data is $(1.56 \pm 0.11) \times 10^{-12}$ erg s $^{-1}$ cm $^{-2}$, and for the combined *XMM-Newton* data is $(3.22 \pm 0.27) \times 10^{-13}$ erg s $^{-1}$ cm $^{-2}$. These values correspond to a total intrinsic X-ray luminosity of $(1.86 \pm 0.13) \times 10^{39}$ erg s $^{-1}$ from the *Chandra* data and $(3.83 \pm 0.33) \times 10^{38}$ erg s $^{-1}$ from the *XMM-Newton* data for our assumed distance of 3.15 Mpc. In both cases, these values are higher than the results obtained from earlier *ROSAT* and *Einstein* data but the differences are explained by the higher fitted column densities of the more recent data. The fraction of the emission due to the individual components is 15% - cooler thermal, 25% - hotter thermal and 60% - power-law from the *Chandra* data and 40% - cooler thermal, 50% - hotter thermal and 10% - power-law from the *XMM-Newton* data. The very high fitted column density for the power-law component in the *Chandra* data accounts for a lot of this discrepancy. The differences in the calibration between the MOS1 camera and the other two *XMM-Newton* cameras will also lead to possible discrepancies when comparing results from the combined *XMM-Newton* fits to *Chandra* fits. We do however note the *Chandra* calibration problems at low energy, which may affect matters at low energies. An important point is that the discrepancies between fits to the *XMM-Newton* and *Chandra* data are much smaller for the two thermal components, and it is these components that we concentrate on in this paper.

3.2 Point Sources

A background subtracted spectrum was extracted from the *Chandra* data for each of the 17 sources within the D_{25} ellipse. (The background spectra were taken from the aforementioned CXC background file and were appropriately scaled. The use of the background files meant that the background spectrum was taken from the identical position on the CCD and avoided the problem of contamination from adjacent sources, which as shown in Fig. 1 is particularly a problem in the central region of NGC 5253.) The spectra were grouped so that each had a minimum of 5 data bins and when possible a minimum of 10 counts per bin. (In fact, due to the low statistics, this was only possible in the case of sources 9, 19, 21 and 22.) No attempt was made initially to fit the data where a source had less than 50 counts after background subtraction. Source 21 has the highest count-rate by far of any of the sources (see Table 2) and is fitted well by an absorbed two component (mekal plus power-law) fit. Galactic absorption is assumed to be $N_{H(GAL)} = 3.87 \times 10^{20}$ cm $^{-2}$ and the metallicity of the X-ray emitting gas is fixed at $0.13Z_{\odot}$ [the average value fitted to the total X-ray emission from NGC 5253, which is

slightly lower than, but agrees within errors with, the value of $0.19 \pm 0.08 Z_{\odot}$ obtained for the HII regions in the centre of NGC 5253 by Webster & Smith (1983)]. The fitted spectrum for this source is shown in Fig. 6 and the fitted parameters are summarised in Table 4 along with those for the other 16 sources within the D_{25} ellipse. Where possible, the other sources were fitted with this same model unless the normalisation went to zero for one of the components, in which case that component was omitted and these fits are indicated by a dash in the parameter values in Table 4. As suggested by Strickland & Stevens (1999), from analysis of the *ROSAT* HRI data for this galaxy, some of the sources detected in the central region of NGC 5253 may be due to superbubbles surrounding super star-clusters rather than individual point sources, such as X-ray binaries. Two of these five sources found by Strickland & Stevens (1999) have been further resolved into two sources using the superior resolution of *Chandra*. We can relate the HRI sources recorded in Strickland & Stevens (1999) to the *Chandra* sources found here as follows: *ROSAT* source A corresponds to source 21, B to source 22, C to source 20, D to sources 18/19 and E to sources 16/17. The assertion that these sources could be extended superbubbles is supported by the source detections here where in particular, sources 16, 17, 18, 19 and 20 are all detected as being elliptical whereas the PSFs at the corresponding positions on the CCD are all circular. The inclusion of a thermal component in the spectral fits for these sources is then to be expected and in the cases of sources 16, 17, 18 and 20, the thermal components completely dominate the spectra. Source 21 appears to be substantially more luminous in this *Chandra* observation than in the *ROSAT* HRI observation, though a detailed comparison is difficult because of the low source counts in the HRI observation.

From the best fits to all the sources within the D_{25} ellipse, the absorption corrected fluxes and luminosities in the 0.3 – 8.0 keV energy band were determined. These luminosities are also included in Table 4 and the $\log(N) - \log(L_X)$ plot for the 17 sources possibly associated with NGC 5253 is shown in Fig. 7. This has been fitted with a single power-law, with a slope of -0.54 ± 0.21 for the higher luminosity sources. Sources with luminosities below an absorption corrected luminosity of 1.46×10^{37} erg s $^{-1}$ were not included in the fit, as these figures represent the completeness limit for the data. The sources where the thermal component dominates are included in this data, even though these may represent the emission from young superbubbles rather than point sources. The slope determined for all the sources is not quite as steep (though comparable to within the errors) as the -0.70 found for NGC 4214 (Hartwell et al. 2003) but slightly steeper than the -0.51 found for NGC 4449 (Summers et al. 2003). As a further comparison, Martin et al. (2002) give an upper limit of -0.55 for the slope of the luminosity function of sources detected in the 1.1 – 6.0 keV energy band in NGC 1569, but also state that the value is not well constrained. The low source counts in the NGC 5253 data make anything more rigorous than a statement of the slope values impossible. The NGC 5253 value is steeper than the value quoted (~ -0.45) by Zelas et al. (2001) for the larger starburst galaxies, M82 and the Antennae. The steeper slopes seen in the dwarfs may be the result of them having fewer high luminosity sources, and in the case of NGC 5253 this could be directly related to it being a younger starburst. (For more analysis of the

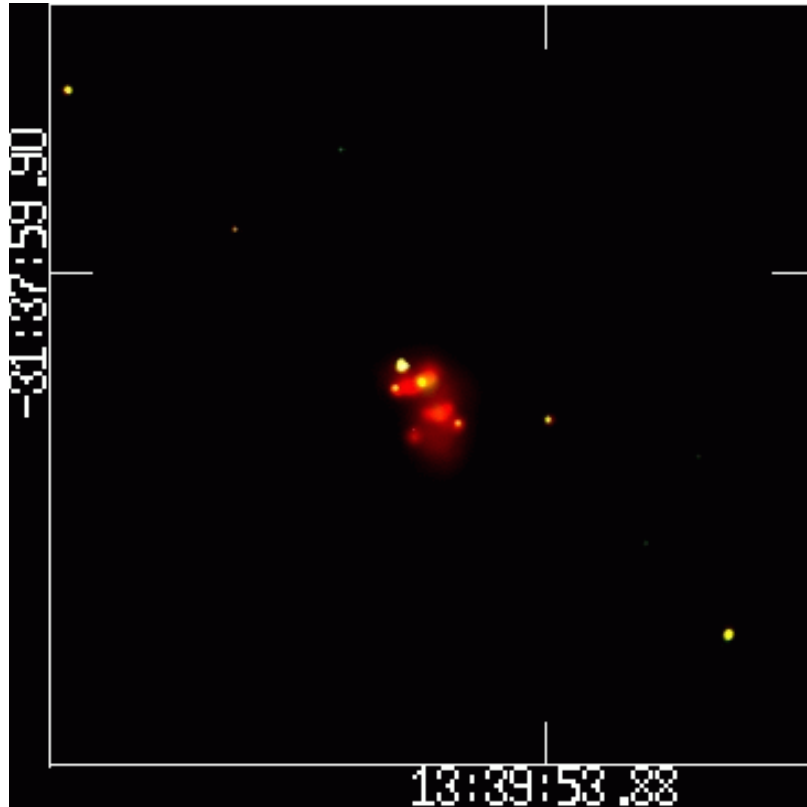


Figure 4. Adaptively smoothed 3 colour image of a 3 arcmin square region of the *Chandra* ACIS-S3 chip, centred on the nucleus of NGC 5253 at $\alpha = 13^h 39^m 56.2^s$, $\delta = -31^\circ 38' 29.9''$ (red: $0.3 - 1.10$ keV, green: $1.10 - 3.80$ keV and blue: $3.80 - 8.0$ keV). The hardness variation in the source spectra is evident, while the diffuse emission is seen to be predominantly soft.

Table 3. Best fits to the background subtracted spectra of the total X-ray emission from within the D_{25} ellipse of NGC 5253 for a $wabs_{GAL}(wabs(mekal) + wabs(mekal) + wabs(po))$ model, with the Galactic column $wabs_{GAL} = 3.87 \times 10^{20} \text{ cm}^{-2}$. The five columns of results proceeding from left to right are for the *Chandra* ACIS-S3 chip, the individual *XMM-Newton* MOS1, MOS2 and PN cameras and the combined results from the data for the three *XMM-Newton* cameras fitted simultaneously. Row 1 lists the individual instruments, rows 2, 4, and 7 are the fitted column densities for the three components, $N_{H(1)}$, $N_{H(2)}$ and $N_{H(3)}$ respectively. Rows 3 and 5 are the temperatures, kT_1 and kT_2 of the two thermal components and row 6 is the fitted metallicity of the X-ray emitting gas, fitted simultaneously for the two thermal components. Row 8 gives the photon index, Γ , of the power-law component, while row 9 gives the fit statistics.

Instrument	Chandra ACIS-S	XMM-Newton			
		MOS1	MOS2	PN	3 XMM
$N_{H(1)} (\times 10^{21} \text{ cm}^{-2})$	1.01 ± 0.12	1.00 ± 0.43	0.89 ± 0.31	0.79 ± 0.12	0.48 ± 0.09
kT_1 (keV)	0.25 ± 0.01	0.26 ± 0.02	0.22 ± 0.02	0.22 ± 0.01	0.25 ± 0.01
$N_{H(2)} (\times 10^{21} \text{ cm}^{-2})$	3.84 ± 0.34	2.06 ± 0.67	1.34 ± 0.70	0.82 ± 0.28	3.78 ± 0.36
kT_2 (keV)	0.76 ± 0.04	0.64 ± 0.08	0.59 ± 0.06	0.73 ± 0.06	0.67 ± 0.04
$Z (Z_\odot)$	0.13 ± 0.01	0.16 ± 0.02	0.11 ± 0.01	0.13 ± 0.01	0.11 ± 0.01
$N_{H(3)} (\times 10^{21} \text{ cm}^{-2})$	46.4 ± 6.04	0.51 ± 1.44	5.00 ± 13.10	8.77 ± 7.31	7.01 ± 30.09
Γ	1.69 ± 0.06	3.60 ± 0.78	2.12 ± 1.68	1.92 ± 0.47	1.54 ± 0.82
$\chi^2/\text{d.o.f.}$	206/150	66/53	71/66	159/145	323/284

luminosity functions of these and other starburst galaxies see Hartwell et al. 2003). The effect of omitting the sources dominated by thermal emission which are probable young superbubbles (sources 16, 17, 18, 19 and 20) is to decrease the slope of the fit to -0.41 , which is more in line with the other results quoted above. This highlights the fact that avoiding source confusion is crucial to this type of analysis and the inclusion of super star-clusters within superbubbles,

as point sources biases the results in such a way as to steepen the slope of the point source luminosity function.

We note that Colbert et al. (2004) in their analysis of the NGC 5253 data, quote a steeper value for the point source luminosity function of -0.92 . A major difference between this and that analysis is that here we fit the spectrum of each source individually (Table 4), whereas Colbert et al. (2004) determine source fluxes using a power-law model with

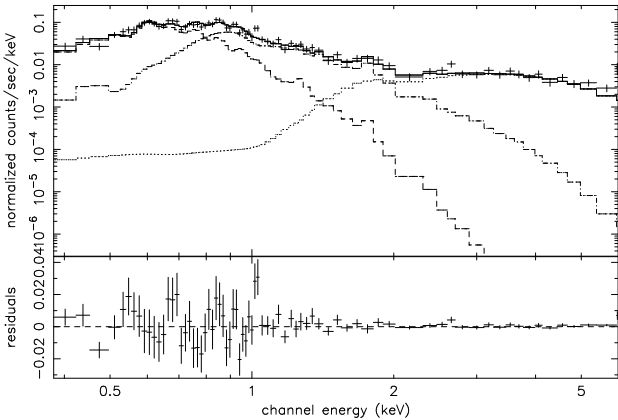


Figure 5. Fitted spectrum of the total X-ray emission from NGC 5253 Left panel: *Chandra* data, right panel: simultaneous fit to the data from the three *XMM-Newton* cameras. The fit is for an absorbed two temperature plus power-law fit, with a column density of $N_H(GAL) = 3.87 \times 10^{20} \text{ cm}^{-2}$ assumed for Galactic absorption. See Table 3 and text for details of the individual fits. The individual contributions from the separate components are shown on the *Chandra* data.

a fixed slope and a column set at the Galactic absorption level. This may well explain the different slopes determined for NGC 5253.

The data were point source searched in the three different energy bands used to produce the three colour image, (soft 0.3 – 1.1 keV, medium 1.1 – 3.8 keV and hard 3.8 – 8.0 keV) and in the three energy bands used for the analysis of NGC 4449 (soft 0.3 – 0.8 keV, medium 0.8 – 2.0 keV and hard 2.0 – 8.0 keV) so that a direct comparison could be made of the sources in the two galaxies. The hardness ratios for the individual sources within the D_{25} ellipse were calculated for the sources detected in more than one of the energy bands. Due to the low count rates for many of the sources most were detected in only 1 or 2 bands. The total counts in each of these energy bands and the calculated hardness ratios are shown in Tables 5 and 6, for the two different sets of energy bands. Note, that when point source searching was carried out in the separate energy bands, sources 18 and 19 when detected as a single source rather than two sources as in the broadband searching. The two hardness ratios shown are $(m-s)/(m+s)$ and $(h-m)/(h+m)$, where s , m and h are the counts in the soft, medium and hard bands respectively. It is noticeable, particularly in Table 5, that the sources in the central region (sources 16-20) are all very soft, with very few counts above 1.0 keV and virtually none above 2.0 keV, suggesting that these are associated with the emission from superbubbles surrounding super star-clusters rather than individual harder objects like X-ray binaries.

In general, the sources detected in NGC 5253 are softer than those in NGC 4449 and lie behind an on average higher absorbing column density. The implication of this being that the sources in NGC 5253 must be softer as the higher column density would preferentially absorb the softer X-ray emission. The low counts for the sources in NGC 5253 will effect these results too, but still, only 5 out of 17 sources have detections in the 2.0 – 8.0 keV band compared with 15 out of 24 for NGC 4449. To better compare some of these sources, the sources where hardness ratios can be calculated from the NGC 5253 data, in the 0.3 – 0.8 keV, 0.8 – 2.0 keV

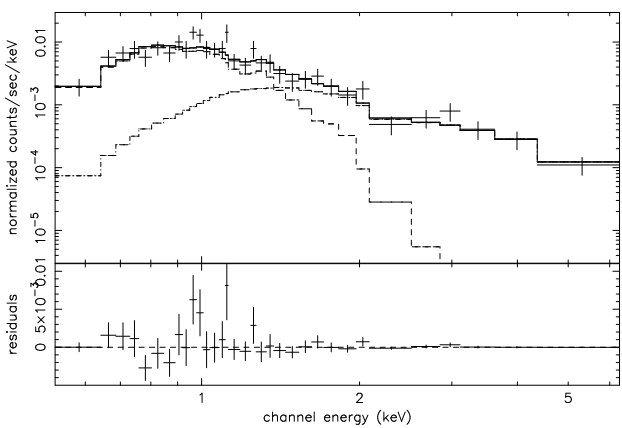
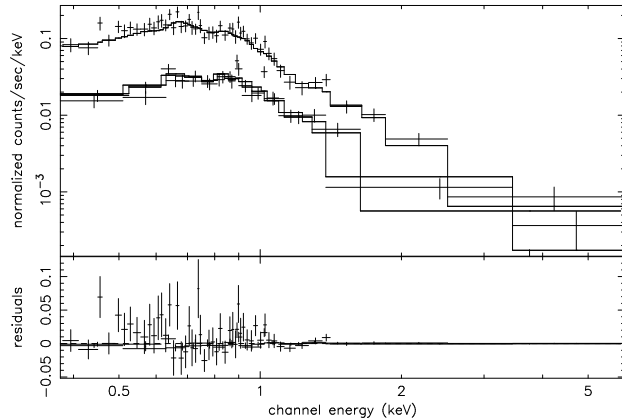


Figure 6. Spectral fit obtained for source 21, the most luminous source in the *Chandra* data. The fit is an absorbed two component (mekal+power-law) fit with the Galactic column density assumed to be $3.87 \times 10^{20} \text{ cm}^{-2}$ and the metallicity fixed at $0.13 Z_{\odot}$ (the average fitted value from the fits to the total emission). The best fit gives $N_H = (8.56 \pm 0.40) \times 10^{21} \text{ cm}^{-2}$, $kT = 0.24 \pm 0.01 \text{ keV}$ and the photon index, $\Gamma = 2.09 \pm 0.19$.

and 2.0 – 8.0 keV energy bands, have been overlaid on the hard vs. soft hardness ratio plot for NGC 4449. The results are shown in Fig. 8 where the NGC 4449 data is shown in black and that for NGC 5253 is in red. The sources represented by squares with arrows, to the right and bottom of the plot, were only detected in 2 of the 3 energy bands and so their positions represent the most extreme positions possible for them on this plot.

The average fitted column density for the NGC 4449 sources is $\sim 3.0 \times 10^{21} \text{ cm}^{-2}$ while that for the NGC 5253 sources is $\sim 7.5 \times 10^{21} \text{ cm}^{-2}$. The effect of these differing values on a plot such as Fig. 8 is to displace the sources towards the right and slightly towards the top of the plot, as the absorbing column behind which they lie increases. For a truer comparison, the NGC 5253 plotted values would decrease by ~ 0.2 – 0.3 in the $(m-s)/(m+s)$ ratio and

Table 4. Results of fitting a *wabsGAL* (*wabs(mekal+po)*) model (the best fit model for source 21) to all 17 sources within the D_{25} ellipse. Column 1 gives the source numbers as shown on Fig. 1. Column 2 contains the fitted column density for each source assuming a Galactic column density of $N_H(GAL) = 3.87 \times 10^{20} \text{ cm}^{-2}$. Columns 3 and 4 contain the temperature of the *mekal* component and photon index of the power-law component respectively. Column 5 and 6 show the absorption corrected flux and luminosity for each source. The errors shown are the 90% confidence regions for each parameter.

Source	N_H ($\times 10^{21} \text{ cm}^{-2}$)	kT (keV)	Γ	Unabsorbed Flux ($\times 10^{-14} \text{ erg s}^{-1} \text{ cm}^{-2}$)	Unabsorbed Luminosity ($\times 10^{38} \text{ erg s}^{-1}$)
9	4.48 ± 1.24	0.08 ± 0.01	1.94 ± 0.40	25.7 ± 15.0	3.06 ± 1.79
10	7.91 ± 7.04	0.25 ± 0.07	1.99 ± 0.23	0.52 ± 0.11	0.06 ± 0.07
11	7.84 ± 1.31	0.23 ± 0.06	1.45 ± 0.34	1.70 ± 1.40	0.20 ± 0.17
13	44.59 ± 24.53	0.25 ± 0.03	1.52 ± 4.25	6.10 ± 5.50	0.73 ± 0.66
15	5.02 ± 1.84	0.25 ± 0.07	2.99 ± 1.37	1.40 ± 0.90	0.17 ± 0.11
16	6.18 ± 1.04	0.17 ± 0.01	—	12.6 ± 3.60	1.50 ± 0.49
17	5.52 ± 1.21	0.25 ± 0.02	—	4.00 ± 1.10	0.48 ± 0.13
18	5.33 ± 1.00	0.24 ± 0.02	—	4.50 ± 1.20	0.54 ± 0.14
19	6.84 ± 0.99	0.24 ± 0.02	1.41 ± 0.93	9.10 ± 2.40	1.08 ± 0.29
20	3.99 ± 1.16	0.22 ± 0.02	—	2.10 ± 0.70	0.25 ± 0.08
21	8.56 ± 0.70	0.24 ± 0.01	2.09 ± 0.19	85.3 ± 10.8	10.0 ± 1.30
22	5.35 ± 0.70	0.15 ± 0.01	2.50 ± 5.23	24.9 ± 6.40	2.96 ± 0.76
24	1.43 ± 0.50	0.08 ± 0.02	1.22 ± 2.83	0.37 ± 0.44	0.04 ± 0.05
25	2.28 ± 1.04	0.18 ± 0.06	2.50 ± 3.80	0.43 ± 0.35	0.05 ± 0.07
26	0.84 ± 1.33	0.15 ± 0.02	0.86 ± 1.39	2.10 ± 0.80	0.25 ± 0.10
27	4.56 ± 10.75	—	1.12 ± 0.58	1.10 ± 0.40	0.13 ± 0.05
29	7.13 ± 3.39	0.29 ± 0.07	0.70 ± 0.82	1.60 ± 1.10	0.19 ± 0.13

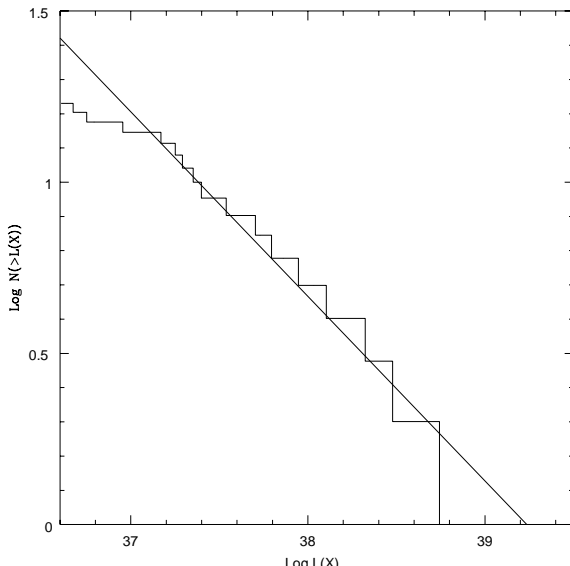


Figure 7. $\log(N) - \log(L_X)$ plot for the 17 point sources detected within the D_{25} ellipse of NGC 5253. The L_X values are absorption corrected and have been fitted as shown in Table 4. The line shown is the power-law fit to the high luminosity end of the data, with a slope of -0.54 ± 0.21 . Incompleteness occurs at an absorption corrected luminosity of $1.46 \times 10^{37} \text{ erg s}^{-1}$.

~ 0.1 in the $(h - m)/(h + m)$ ratio, if the average column density of NGC 4449 was assumed. Of the 5 sources detected in the 2.0 – 8.0 keV band, two of them (sources 10 and 27) along with source 13, which in addition has a very high fitted column density, have spectra that show no emission below 1.0 keV. As such, these three sources are possible candidates for background AGN. These figures are in good agreement

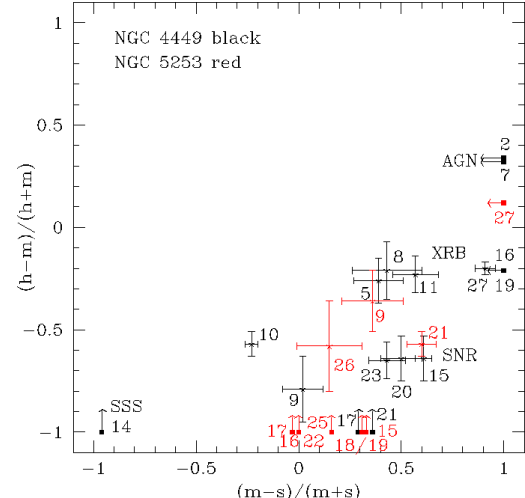


Figure 8. Hard vs. soft hardness ratios for the sources detected in the separate energy bands. The data shown in black are for NGC 4449 (Summers et al. 2003) and in red for NGC 5253. The hard hardness ratio is calculated from the 2.0 – 8.0 keV and 0.8 – 2.0 keV energy bands and the soft hardness ratio is calculated from the 0.8 – 2.0 keV and 0.3 – 0.8 keV energy bands, in the usual way, as defined in the headings of columns 5 and 6 of Table 6. An indication of the likely origin of the sources depending on their location in this plot is shown by labels placed next to the identified sources in the NGC 4449 data. The sources plotted with squares to the right and bottom were only detected in 2 out of the 3 energy bands. The arrows indicate the direction that the sources would move if higher count rates permitted detections in all three energy bands. The error bars have also been omitted from these sources to avoid additional confusion on the plot. See Table 6 for those associated with NGC 5253.

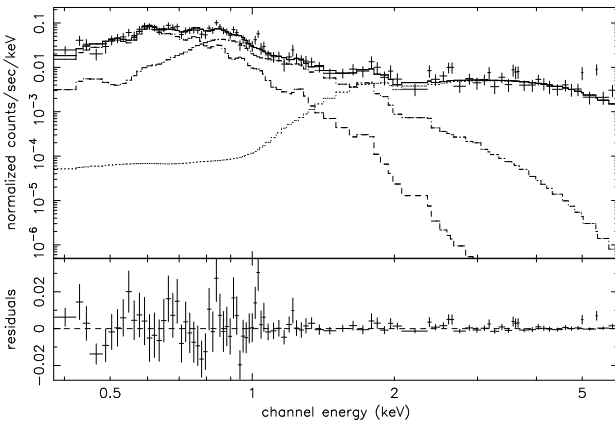


Figure 9. Fitted spectrum of the NGC 5253 diffuse emission as seen with *Chandra*. The fit is an absorbed two temperature plus power-law fit, with assumed Galactic column density of $N_{H(GAL)} = 3.87 \times 10^{20} \text{ cm}^{-2}$. The fitted temperature components were 0.24 ± 0.01 and $0.75 \pm 0.05 \text{ keV}$, with fitted absorbing column densities of $(0.96 \pm 0.13) \times 10^{21} \text{ cm}^{-2}$ and $(1.96 \pm 0.34) \times 10^{21} \text{ cm}^{-2}$ respectively. The metallicities for the two thermal components were fitted simultaneously giving a value of $0.14 \pm 0.01 Z_{\odot}$. The fitted absorbing column density and photon index of the power-law component were $(3.74 \pm 0.44) \times 10^{22} \text{ cm}^{-2}$ and $\Gamma = 1.43 \pm 0.06$ respectively.

with the number of background sources that would be expected within the D_{25} ellipse from ‘The *Chandra* Deep Field South Survey’ (Campana et al. 2001) for our completeness limit (~ 2 for our completeness limit and up to ~ 7 down to a flux level corresponding to that of our faintest detected source).

The three sources detected in all three energy bands (Sources 9, 21 and 26), along with sources 11 and 29, which were only detected in the medium band, are most likely X-ray binaries as none of these sources are coincident with the positions of the reported supernova explosions in NGC 5253 in 1895 and 1972 (1895B: $\alpha = 13^h 39^m 57.4^s$, $\delta = -31^{\circ} 38' 06''$; 1972E: $\alpha = 13^h 39^m 52.6^s$, $\delta = -31^{\circ} 40' 10''$, Caldwell & Phillips 1989) In fact, none of the detected sources tie up with the reported positions. Source 21 lies closest to the reported position of SN1895B (18 arcsec to the SW of its position) and source 11 lies closest to that for SN1972E (15 arcsec WSW of its position).

3.3 Diffuse Emission

A background and point source subtracted spectrum of the region containing the diffuse emission was extracted from the *Chandra* data only, as the spatial resolution of *XMM-Newton* was inadequate for resolving the point sources within the central region. This diffuse emission spectrum is shown in Fig. 9. The fitted model shown is an absorbed three component fit having two thermal components and a power-law component - $wabs_{GAL}(wabs(mekal) + wabs(mekal) + wabs(po))$. The fit gives $N_H = (0.96 \pm 0.13) \times 10^{21} \text{ cm}^{-2}$, $(1.96 \pm 0.34) \times 10^{21} \text{ cm}^{-2}$ and $(3.74 \pm 0.44) \times 10^{22} \text{ cm}^{-2}$, for the fitted absorbing column densities of the cool, warm and power-law components respectively. The fitted temperatures are $kT \sim 0.24 \pm 0.01 \text{ keV}$ for the soft component, and

$kT \sim 0.75 \pm 0.05 \text{ keV}$ for the medium component, while the fitted photon index for the power-law component is $\Gamma = 1.43 \pm 0.06$. The metallicities for the two thermal components were fitted simultaneously, with $0.14 \pm 0.01 Z_{\odot}$.

The absorption corrected fluxes (and percentage contributions) in the $0.37 - 6.0 \text{ keV}$ energy band in each of these three components were: cool thermal: $(1.84 \pm 0.13) \times 10^{-13} \text{ erg s}^{-1} \text{ cm}^{-2}$ (20%); warm thermal: $(1.47 \pm 0.13) \times 10^{-13} \text{ erg s}^{-1} \text{ cm}^{-2}$ (15%) and power-law: $(6.48 \pm 0.58) \times 10^{-13} \text{ erg s}^{-1} \text{ cm}^{-2}$ (65%). The errors shown here are the 90% confidence levels for the normalisation value obtained from the fit. This result suggests that the diffuse emission consists of at least two components at different temperatures and many unresolved point sources.

As discussed in Section 3.1, several of the point sources in the central region of NGC 5253 could be young superbubbles and the subtraction of such sources could therefore remove a substantial fraction of the diffuse emission. Comparing the fluxes above with those obtained from the analysis of the total emission gives the result that the point source subtraction has removed $\sim 25\%$ of the cool thermal emission, $\sim 60\%$ of the warmer thermal emission and 35% of the emission attributed to the power-law component, but these figures do not take account of the fact that the fitted values for the absorbing column densities have changed between the two fits. Re-fitting the diffuse emission with the values fitted for the total emission and only allowing the normalisations for the individual components to be free gives reductions in the fluxes that correspond to $\sim 12\%$ for the cool thermal emission, $\sim 46\%$ for the warmer thermal emission and $\sim 14\%$ for the emission from the power-law component. This does suggest that the cooler thermal component is affected less by the point source subtraction and so probably lies further away from the point sources and star-clusters than the warmer component. When sources 16, 17, 18 and 20 are not subtracted from the total emission and this modified emission is fitted as above with only the normalisations of each component as free parameters, the reduction in the fluxes for each component are: cool thermal: $\sim 10\%$; warm thermal: $\sim 43\%$; power-law: $\sim 13\%$. These figures suggest there is emission from all three components of the fit associated with these four sources, with maybe slightly more of the warmer thermal component than the other two, and yet the temperatures measured for them during the spectral fitting was of the order of that of the cooler component. As their contribution is not a substantial fraction of the total emission in all three components, their inclusion in the source subtraction does not effect the fluxes measured for the diffuse emission greatly.

Other parameters of the two gas components have been calculated, from the spectral fits to the *Chandra* data for the diffuse emission and the *XMM-Newton* data for the total emission. The results are shown in Table 7, including the effect of a filling factor f , and within errors most of the calculated values agree between the two data sets. The implications of these figures for the evolution of NGC 5253 will be discussed further in Section 4. The assumption of spherical symmetry and a filling factor of unity are both likely to be overestimates, resulting in the quoted figures being underestimates for n_e and P and overestimates for M , E_{Th} and t_{cool} (see Strickland & Stevens 2000 for a discussion of filling factors and their likely values in galactic winds).

Table 5. Hardness ratios for the 17 sources detected within the D_{25} ellipse. Soft band, s , 0.3 – 1.1 keV, medium band, m , 1.1 – 3.8 keV and hard band, h , 3.8 – 8.0 keV. Where no counts are shown, *wavdetect* failed to detect the object in that energy band. Column 1 gives the source numbers as shown on Fig. 1. Columns 2 – 4 are the counts in the 3 different energy bands and columns 5 and 6 give the values of the hardness ratios calculated as detailed in the column headings.

Source	Counts in Soft Band (0.3 – 1.1 keV)	Counts in Medium Band (1.1 – 3.8 keV)	Counts in Hard Band (3.8 – 8.0 keV)	$\frac{(m - s)}{(m + s)}$	$\frac{(h - m)}{(h + m)}$
9	31.1 ± 5.7	36.1 ± 6.2	-	0.07 ± 0.13	-
10	-	6.1 ± 2.6	7.9 ± 3.0	-	0.13 ± 0.29
11	7.3 ± 2.8	12.7 ± 3.7	-	0.27 ± 0.24	-
13	-	7.6 ± 2.8	-	-	-
15	16.0 ± 4.2	13.0 ± 3.7	-	-0.10 ± 0.19	-
16	28.0 ± 7.1	-	-	-	-
17	27.1 ± 7.0	-	-	-	-
18/19	43.4 ± 8.9	28.7 ± 6.5	-	-0.20 ± 0.16	-
20	29.7 ± 7.6	-	-	-	-
21	182.2 ± 14.2	190.9 ± 14.1	23.0 ± 4.9	0.02 ± 0.05	-0.79 ± 0.09
22	63.3 ± 9.2	12.2 ± 4.1	-	-0.68 ± 0.16	-
24	-	-	-	-	-
25	7.5 ± 2.8	7.9 ± 2.8	-	0.03 ± 0.26	-
26	23.0 ± 4.9	20.0 ± 4.6	-	-0.07 ± 0.16	-
27	-	34.4 ± 6.0	-	-	-
29	9.4 ± 3.2	9.7 ± 3.4	-	0.02 ± 0.25	-

Table 6. Hardness ratios for the 17 sources detected within the D_{25} ellipse. Soft band, s , 0.3 – 0.8 keV, medium band, m , 0.8 – 2.0 keV and hard band, h , 2.0 – 8.0 keV. Details as per Table 5. These bands are used for comparison with data for NGC 4449.

Source	Counts in Soft Band (0.3 – 0.8 keV)	Counts in Medium Band (0.8 – 2.0 keV)	Counts in Hard Band (2.0 – 8.0 keV)	$\frac{(m - s)}{(m + s)}$	$\frac{(h - m)}{(h + m)}$
9	17.3 ± 4.2	36.6 ± 6.2	17.1 ± 4.4	0.36 ± 0.15	-0.36 ± 0.15
10	-	-	14.3 ± 4.4	-	-
11	-	10.5 ± 3.3	-	-	-
13	-	-	-	-	-
15	8.9 ± 3.2	17.7 ± 4.4	-	0.33 ± 0.22	-
16	17.4 ± 5.1	17.3 ± 5.4	-	0.00 ± 0.22	-
17	24.0 ± 6.3	22.5 ± 6.8	-	0.03 ± 0.20	-
18/19	23.6 ± 6.2	44.5 ± 8.6	-	0.31 ± 0.16	-
20	16.1 ± 5.3	-	-	-	-
21	66.2 ± 9.0	264.2 ± 16.7	73.0 ± 8.7	0.60 ± 0.07	-0.57 ± 0.06
22	39.6 ± 7.2	39.9 ± 7.3	-	0.00 ± 0.14	-
24	-	-	-	-	-
25	5.6 ± 2.4	7.8 ± 2.8	-	0.16 ± 0.28	-
26	16.7 ± 4.1	22.8 ± 4.9	6.1 ± 2.6	0.15 ± 0.16	-0.58 ± 0.22
27	-	17.0 ± 4.2	21.7 ± 4.8	-	0.12 ± 0.17
29	-	12.9 ± 3.6	-	-	-

Overall, the metallicity of the hot X-ray emitting gas is similar to that obtained from optical spectroscopy of the central HII regions (Webster & Smith 1983) of the galaxy. Compared to other dwarf galaxies though, the values of $0.14 \pm 0.01 Z_{\odot}$ from the diffuse X-ray data and $0.19 \pm 0.08 Z_{\odot}$ from the optical data are low. Typical values for some other dwarfs are: Mrk 33: $\sim 0.3 Z_{\odot}$ (Legrand et al. 1997); NGC 4449: $\sim 0.32 \pm 0.08 Z_{\odot}$ for the X-ray emitting gas (Summers et al. 2003); NGC 1569: $> 0.25 Z_{\odot}$ for the X-ray emitting gas and a mean value of $0.2 Z_{\odot}$ for the ISM material (Martin et al. 2002). In a further attempt to investigate the metallicities of the thermal components, and in particular the ratio of the α -elements to Fe, the spectrum was

re-fitted using variable abundance mekal models (*vmekal*) for the two thermal components. The abundances of the two thermal components were tied and the individual abundances of Mg, Ne, Si and Ca relative to Solar values were tied to that of O to form the group of α -elements. The abundances of all the other elements were set to the global value determined above. The α/Fe ratio obtained in this way was found to have no significant difference to the Solar value at $(1.05 \pm 0.30)(\alpha/Fe)_{\odot}$. The confidence contour plot for these fits is shown in Fig. 10, showing that the α and Fe abundances are highly correlated, and that the fitted ratio is ~ 1 . We note that this is somewhat in contrast to the values of Martin et al. (2002) for the dwarf starburst NGC 1569,

Table 7. The gas parameters for the two thermal components of the diffuse emission. The assumptions made are that the volume of the emitting region is $V = 1.54 \times 10^{64} \text{ cm}^3$ (assuming spherical symmetry); $D = 3.15 \text{ Mpc}$; a filling factor, f ; $n_e \sim (EI/Vf)^{1/2}$ where EI is the emission integral ($\text{norm} \times 4\pi D^2)/10^{-14}$ and norm is the normalisation obtained from the spectral fitting; $P \sim 2n_e kT$, $M \sim n_e m_p Vf$, $E_{Th} \sim 3n_e kTV$ and $t_{cool} \sim (3kT)/(\Lambda n_e)$ where $\Lambda = L_X/EI$. Columns 2 and 3 give the values calculated from the *Chandra* data while columns 4 and 5 are the corresponding *XMM-Newton* values.

	<i>Chandra</i>		<i>XMM-Newton</i>	
	Soft component	Medium component	Soft component	Medium component
kT (keV)	0.24 ± 0.01	0.75 ± 0.05	0.25 ± 0.02	0.67 ± 0.04
T (10^6 K)	2.78 ± 0.12	8.69 ± 0.58	2.90 ± 0.11	7.76 ± 0.47
L_X ($10^{38} \text{ erg s}^{-1}$)	2.19 ± 0.16	1.75 ± 0.15	1.65 ± 0.08	1.82 ± 0.14
n_e [$\times f^{1/2}$] (cm^{-3})	0.065 ± 0.002	0.041 ± 0.001	0.060 ± 0.001	0.044 ± 0.002
E_{Th} [$\times f^{1/2}$] (10^{54} erg)	1.15 ± 0.06	2.25 ± 0.18	1.11 ± 0.06	2.21 ± 0.16
M [$\times f^{1/2}$] (10^6 M_\odot)	0.84 ± 0.03	0.53 ± 0.03	0.78 ± 0.01	0.58 ± 0.03
P [$\times f^{-1/2}$] ($10^{-11} \text{ dyn cm}^{-2}$)	4.97 ± 0.30	9.79 ± 0.75	4.82 ± 0.20	9.59 ± 0.70
t_{cool} [$\times f^{1/2}$] (10^8 yr)	1.67 ± 0.19	4.13 ± 0.62	2.15 ± 0.16	3.82 ± 0.50
Λ ($10^{-24} \text{ erg s}^{-1} \text{ cm}^3$)	3.36 ± 0.34	6.78 ± 0.84	2.95 ± 0.19	5.95 ± 0.65
EI (10^{61} cm^{-3})	6.52 ± 0.45	2.58 ± 0.23	5.59 ± 0.23	3.06 ± 0.24

where values of the α to Fe abundance ratio of 2.1–3.9 times the Solar value are quoted (and in the case of NGC 1569 the photon statistics are rather better than for NGC 5253). This value for NGC 5253 is more in line with the value of $(0.91 \pm 0.07)(\alpha/Fe)_\odot$ found for the dwarf starburst NGC 4449 (Summers et al. 2003) and may be indicative of differences in the contributions made to the hot gas from SNe in these different starbursts. The high values quoted for NGC 1569 suggest the presence of more Type II SNe, which would be expected if its current starburst phase is $\sim 10 - 20$ Myr old as suggested in the literature on this starburst (e.g., Israel & De Bruyn 1988; González-Delgado et al. 1997; Hunter et al. 2000). Such activity would give rise to more α -elements, as would a pattern of shorter more intense bursts of star formation. The fact that NGC 5253 has shown a fairly uniform rate of star-formation throughout the galaxy over the last $10^8 - 10^9$ yr (Caldwell & Phillips 1989), would suggest that, with the exception of the current burst in the very central region, which could be very young and hence have little Type II SNe activity at present, its star-formation and energy injection from star-forming regions has been generally of a more continuous nature.

From Table 4, it can be seen that there is little temperature variation evident within the sources, that appear to be extended (16, 17, 18, 19 and 20), in the central region of NGC 5253, with the exception of source 16 in the SW being cooler than the rest. The absorbing column densities fitted to them are also fairly consistent and there is overlap seen between adjacent sources within errors. The dust lane in NGC 5253 bisects the nuclear region such that sources 18 and 19 lie to the north of it and sources 16, 17 and 20 are to the south. From the hardness ratios and source counts in various energy bands shown in Tables 5 and 6, the two northern sources are harder than those in the south, suggesting that they should be either hotter or lie behind larger absorbing columns. Source 17's temperature and 16's absorbing column density would argue against this. The latter could be explained by the western side of the galaxy being tilted away from us. The low count-rate statistics however, hamper the drawing of any firm conclusions, though the results do suggest that these objects are similar in nature to each other.

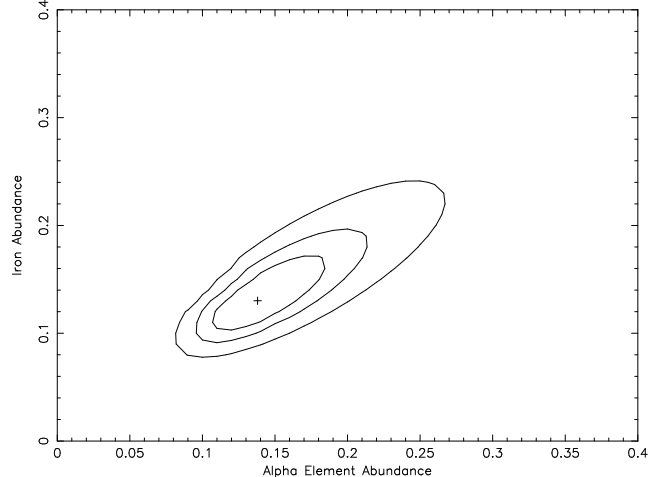


Figure 10. The confidence contours for the α and Fe element abundances (see text for details). The units of both axes are the solar values for the α elements and Fe respectively. The contours shown are the 68%, 90% and 99% contours.

Also, from the 3 colour *Chandra* image, further differences can be seen in the nature of the point sources in these three energy bands. Sources 17, 18, and 20 all appear very red on the three colour image, reinforcing their similar nature. Sources 16 and 19 show slightly different behaviour, by having more emission in the medium band than the other three sources, which is reflected in their yellow colour on Fig. 4. The diffuse emission is mainly confined to the central region of the galaxy, and the peak of its emission is centred on the region occupied by sources 17, 18 and 19, which also corresponds to the region of peak intensity in the $H\alpha$ emission. The images of the *XMM-Newton* data shown in Figs. 2 and 3 show that the diffuse X-ray emission extends away from the central region in several directions, although as stated earlier most of the extension to the SW appears to be associated with point sources. This is confirmed by the log-log plot of the radial surface brightness profile shown in Fig. 11, produced by extracting the counts from 20 concentric annuli each with a width of $2.75''$ cen-

tered on a position coincident with the centre of the D_{25} ellipse at $\alpha = 13^h 39^m 56.2^s$ and $\delta = -31^\circ 38' 29.9''$. This figure shows that the diffuse emission can only be traced out to a distance of $\sim 35''$ (0.53 kpc for our assumed distance) before it falls to a level comparable to that of random background fluctuations. The preferred directions for the observed extensions in the diffuse emission seem to be along the minor axis of the galaxy, both to the NW and SE. If these extension in the diffuse X-ray emission are due to superbubbles and superwinds then their activity should have swept-up shells and produced filaments which should be evident in the $H\alpha$ image of the galaxy. To look for such evidence, of correlations between the extended X-ray emission and structure within the $H\alpha$ emission, X-ray contours from the point source and background subtracted diffuse emission have been overlaid on the $H\alpha$ image of the central region of NGC 5253. In addition, the detected sources in the central region of the galaxy (sources 15–22) are also overlaid on the image to show the relative positions, and extent of these sources (as determined by the *wavdetect* program), compared with the regions of increased star-formation on the $H\alpha$ image. The results are shown in Fig. 12 and the correlations between the various components are discussed further in Section 4.1.1. As a further comparison between emission at different wavebands, Fig. 13 shows the positions of the six largest star clusters found in the central region of NGC 5253 overlaid on the *Chandra* soft (0.3–1.1 keV) and medium (1.1–3.8 keV) smoothed images of the galaxy along with the positions of the X-ray sources 15–22 as shown in Fig. 12. These images show only two strong correlations between the most northern and southern star clusters shown here and X-ray sources. Most of the soft X-ray emission occurs between and around these large star clusters in regions where many smaller clusters are to be found. The second most northern of these large star clusters shown on these images has four smaller clusters in close proximity to it, yet it appears to have little X-ray emission close to it. However, these clusters are located at the western end of the dust lane, which is most likely responsible for the absorption of the X-ray emission seen both in these images and on Fig. 4.

4 DISCUSSION

It is apparent from Fig. 12 that both the diffuse X-ray emission and the $H\alpha$ emission are mainly confined to a region of radius ~ 0.5 kpc in the centre of NGC 5253. The most intense X-ray emission is coincident with the most intense emission seen in the $H\alpha$ image in the Northern half of the nucleus, suggesting that this emission is associated with the increased star-formation occurring in these regions. In general, higher column densities were fitted for the sources to the W and S of the galaxy, as seen in Table 4, and would suggest that these areas lie further away from us behind more absorbing material than the N and E of the galaxy. This would mean the minor axis lies away from our line-of-sight (tilted both to the N and W), and that the galaxy is also rotated about this axis in such a way that the Southern side of the galaxy disk is tilted away from us, consistent with NGC 5253 being a dwarf elliptical galaxy that is inclined to our line-of-sight. The bulging of the diffuse emission seen to the NW and SE in the X-ray contours and *XMM-Newton*

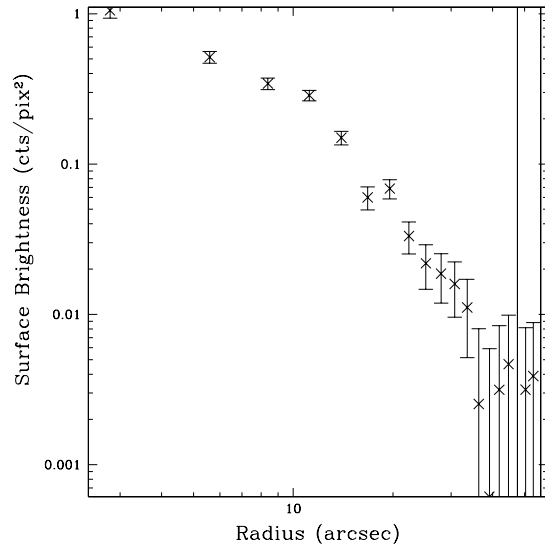


Figure 11. Background subtracted radial surface brightness plot, showing the extent of the diffuse X-ray emission in the 0.3–8.0 keV band. The counts were extracted in 20 concentric annuli, each with a width of $2.75''$ centred on $\alpha = 13^h 39^m 56.2^s$ and $\delta = -31^\circ 38' 29.9''$. The diffuse emission extends out to $\sim 35''$ (~ 0.53 kpc) by which point, the emission has dropped to the background level.

images, could be indicative of a bipolar outflow along the minor axis of the galaxy, as would be expected from standard superbubble models (Weaver et al. 1977).

4.1 Comparison with Observations at Other Wavelengths

4.1.1 $H\alpha$ Emission

NGC 5253 contains many regions of increased star-formation within the central region of the galaxy, which are clearly visible in $H\alpha$ observations, with the most intense regions being seen in the North of the nucleus, coincident with the end of the dust lane and weak CO emission (Turner et al. 1997). This is the region that contains two of the brightest star-clusters analysed by Tremonti et al. (2001) and corresponding to our detected X-ray sources 18 and 19. The extension seen in the diffuse emission to the WNW of this region could be the result of an outflow induced by the stellar winds of the massive stars present in these star clusters. This region also lies close to the position of the ‘radio super-nebula’ discussed by Gorjian et al. (2001), which they have interpreted as an highly obscured, very young globular cluster, rather than an obscured AGN (see also Mohan, Anantharamaiah & Goss 2001; Turner et al. 2003).

As well as many of the star clusters coinciding with X-ray sources, some of the filamentary and shell-like structures seen in $H\alpha$ images seem to have counterparts in the diffuse X-ray emission. The small $H\alpha$ shell seen to the SSE in Fig. 12 appears to be filled with diffuse X-ray emission and the radial filament extending off the $H\alpha$ image to the ESE is also associated with what appears to be a filamentary extension of the diffuse X-ray emission. The field-of-view of the $H\alpha$ image shown in Fig. 12 is too small to show the ~ 1 kpc shells

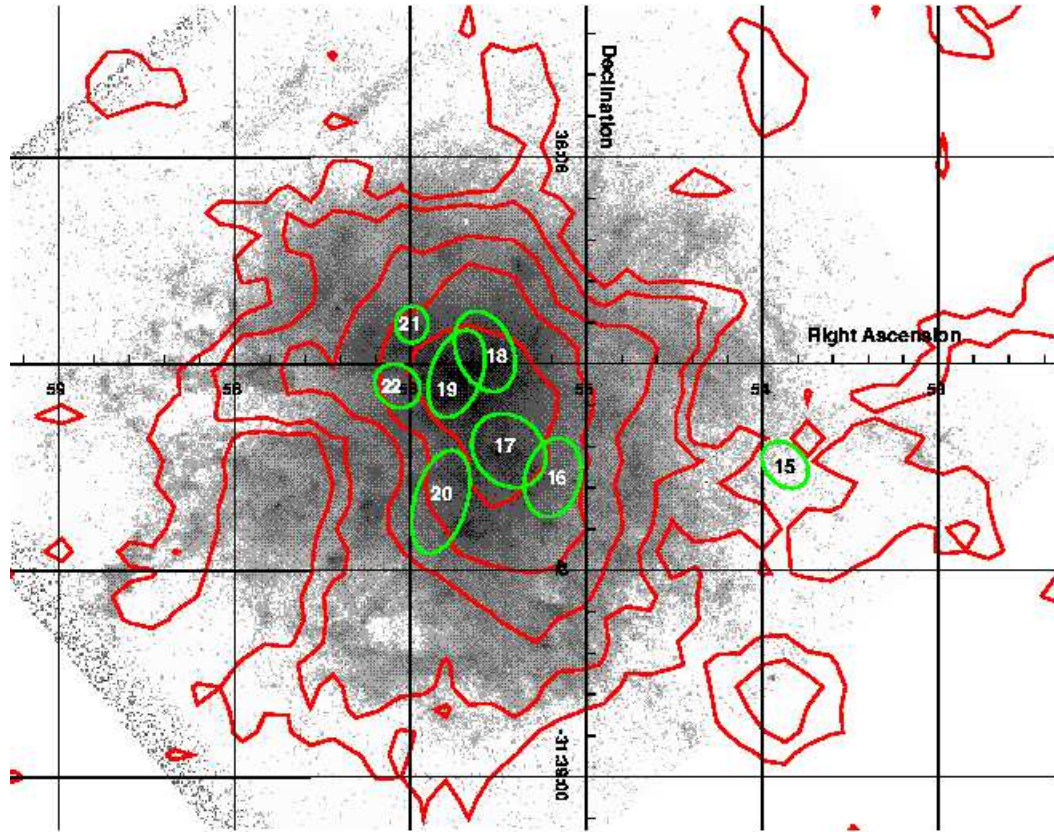


Figure 12. X-ray contours from the *Chandra* diffuse emission (0.3–8.0 keV energy band) overlaid on an H α image of NGC 5253. The X-ray contours shown are at flux densities of 0.26×10^{-13} , 0.52×10^{-13} , 1.04×10^{-13} , 2.08×10^{-13} and 4.16×10^{-13} erg s $^{-1}$ cm $^{-2}$ arcmin $^{-2}$. Also shown are the positions and extent of the sources detected in the central region of the *Chandra* data and these are labelled with their ID numbers as shown in Fig. 1. North is to the top and East to the left.

detected to the West of the galaxy by Marlowe et al. (1995), but these can be seen in Fig. 2j of Martin (1998). The orientation of the more northern of these two shells is roughly aligned with the galaxy's minor axis. The slow expansion speed of these shells [~ 35 km s $^{-1}$] (Marlowe et al. 1995) and the fact that the diffuse X-ray emission does not extend out to them, as shown in the radial surface brightness plot of Fig. 11, may mean that these shells are not associated with the current burst of star formation but are remnants of earlier starburst activity. The presence of more than one bubble having been blown close to the minor-axis on the West side suggests that what is being seen in this galaxy is much more complex than the simple bipolar outflow scenario assumed to explain the effect of starburst activity. This phenomenon could be the result from a young starburst, in so much as the outflows from individual star-clusters may not have overlapped or merged to produce what would be observed as a single outflow. The presence of the dust lane bisecting the nuclear region may also be acting in such a way as to channel any superbubbles so that they expand preferentially into areas where the density of the ambient ISM

is less. The possible dynamics of such superbubbles will be discussed later.

4.1.2 Infrared and Radio Emission

Strong mid-infrared emission (Gorjian et al. 2001) is detected from a source in the northern half of the central region of the galaxy just at the Northern edge of our detected sources 18 and 19. This is an extremely compact source occupying a region with diameter $\sim 1 - 2$ pc and needing to contain $\sim 10^5 - 10^6$ stars to supply its ionization requirements. This object is most likely a very young (no more than a few $\times 10^6$ years old) globular cluster.

Just to the south of this infrared emission, at a position corresponding to our source 19, is the peak of the 2cm radio emission (Beck et al. 1996). While mainly concentrated in the Northern half of the central region of the galaxy, some 2cm emission is also detected at the positions of our sources 17 and 20 but not coincident with source 16. This radio emission has a flat spectrum, with a spectral index of -0.1 ± 0.01 , which is attributed to thermal bremsstrahlung emission from the HII in the region. Relatively low levels of non-thermal

synchrotron emission are seen in NGC 5253 (Turner et al. 1998), which is unusual for a starburst galaxy and again suggests that the starburst occurring in the central region of NGC 5253 could be young.

As mentioned earlier, VLA 21 cm observations of NGC 5253 have suggested that the bulk of the HI rotates about the galaxy's major axis (though see Meier et al. 2002 for evidence of infall into NGC 5253). Fig. 1 of Kobulnicky & Skillman (1995), shows that the neutral gas extends to about twice the optical extent of the galaxy along its minor axis, occupying a region of $\sim 4'$ in diameter. This is well beyond the extent of the diffuse X-ray emission and H α emission seen in the central region. The peculiar rotation could result from large-scale outflow along the minor axis, but such behaviour should give rise to a shell-like centrally evacuated structure in HI emission, as seen in the ~ 1 kpc H α shells. The column density measured for the HI increases towards the centre and peaks at a position close to our detected source 20. This is offset by about $15''$ from the peaks of emission seen at shorter wavelengths and is in the southern rather than northern half of the galaxy, however this does coincide with the point where the dust lane enters the nuclear region from the ESE.

4.2 Potential for Blow-out and its Implications on the Fate of NGC 5253

Although at present there does not appear to be a clearly defined single superbubble structure within NGC 5253, the presence of hot, over-pressured gas with a long cooling time, should lead to an outflow from the central region. With this in mind, in this section we apply the standard superbubble model to the hot gas of NGC 5253 to investigate the potential of the galaxy to deposit energy, metal-enriched material and ISM material into the intergalactic medium.

The age of the current burst of star-formation in the centre of NGC 5253 is not well determined, and probably does not have a single age. The comparative lack of a non-thermal signature in the radio-spectrum (Beck et al. 1996; Turner et al. 1998) may suggest a lack of supernova activity and the detected presence of Wolf-Rayet stars (Schaerer et al. 1997) in regions corresponding to our detected source 19 suggest that star-formation has been occurring for only a few Myr in this region. Typically ages for star clusters in NGC 5253 reported in the literature are: 7.9 Myr (Marlowe et al. 1999); 2.8 Myr and 4.4 Myr for two separate regions within the nucleus (Schaerer et al. 1997); 2 Myr for the brightest star cluster (Tremonti et al. 2001); 5 Myr (Martin & Kennicutt 1995); 3 Myr (Mas-Hesse & Kunth 1999), though as noted earlier there are some older clusters (Calzetti et al. 1997), and indeed these older star-clusters can still be contributing mechanical luminosity.

Based on these figures we adopt an age of 5 Myr for the current starburst, in order to perform some analysis of the dynamics of the probable superbubbles in NGC 5253. We recognise the limitation of this approach in such a complex system as NGC 5253, where the star-formation is not co-eval. The northern star-clusters in NGC 5253 are younger and here the analysis may be useful.

The bulk of the diffuse X-ray emission is confined within a radius of $\sim 0.6'$ (0.53 kpc for our assumed distance), that corresponds to the same region containing the majority of

the H α emission as shown in Fig. 12. For simplicity this will be treated as a single superbubble resulting from the combined action of the multiple star-clusters within the starburst. The dynamic time required for the two ~ 1 kpc H α shells detected by Marlowe et al. (1995) to have evolved is ~ 10 Myr, assuming they have had a constant expansion velocity of 35 km s^{-1} (Marlowe et al. 1995) for this time. This value is greater than the estimated duration of the current burst of star-formation, and the diffuse emission does not appear to extend this far out. However, this figure is also likely to be an over estimate since their speed will have been greater in the past, which would bring their expansion times closer to the higher age estimates of the star clusters. These observations raise the question of what is responsible for their existence which will be discussed further later.

The combined action of the stellar winds of the massive O and B stars in the star-forming regions in the centre of NGC 5253 will blow a superbubble that can be modelled using the starburst driven outflow models of Castor, McCray & Weaver (1975) and Weaver et al. (1977). In such models, the stellar winds from the OB associations sweep up and shock a thin, dense H α emitting shell of ISM material, with a contact discontinuity just behind the shell, separating the shocked wind material from the shocked ISM material. The innermost region of the bubble will contain the freely expanding supersonic wind bounded by an inward-facing shock. In the 'snow-plough' phase, the shocked wind material occupies most of the bubble's interior and most of the bubble's mass is contained in the H α shell. The expansion of the bubble is driven by the over-pressured interior, which, as can be seen from the figures of Table 7 is of an order of magnitude greater than typical values for the ambient ISM within the Milky Way which is $\sim 10^{-12} \text{ dyn cm}^{-2}$. The radius R_B and expansion velocity v_B , of the bubble during this phase, are given by

$$R_B = 168 \left(\frac{L_{\text{mech},40}}{n_0} \right)^{1/5} t_6^{3/5} \text{ pc} \quad (1)$$

$$v_B = 99 \left(\frac{L_{\text{mech},40}}{n_0} \right)^{1/5} t_6^{-2/5} \text{ km s}^{-1}, \quad (2)$$

where $L_{\text{mech},40}$ is the mechanical luminosity injected by the starburst in units of $10^{40} \text{ erg s}^{-1}$, t_6 is the age of the starburst in units of 10^6 yr and n_0 is the ambient atomic number density of the ISM.

The mechanical luminosity (L_{mech}) injected by the starburst can be estimated from the stellar populations in the starburst. Marlowe et al. (1999) have performed a detailed analysis of the starburst in NGC 5253, using starburst evolutionary synthesis models (c.f. Leitherer & Heckman 1995; Leitherer et al. 1999) and they estimate that the energy injection rate in NGC 5253 is $L_{\text{mech}} = 3.6 \times 10^{40} \text{ erg s}^{-1}$ for both instantaneous burst and continuous star-formation models, and we shall adopt this figure hereafter. The mass injection rate from the *Starburst99* models for this level of mechanical luminosity will be $\sim 0.02 - 0.04 M_{\odot} \text{ yr}^{-1}$ depending on whether instantaneous or continuous starburst models are assumed (for an age of 5 Myr).

An estimate of the ambient density in the central regions, n_0 , can be made based on the HI observations of Kobulnicky & Skillman (1995). The peak HI column density in the central regions is $2.6 \times 10^{21} \text{ cm}^{-2}$ which, assum-

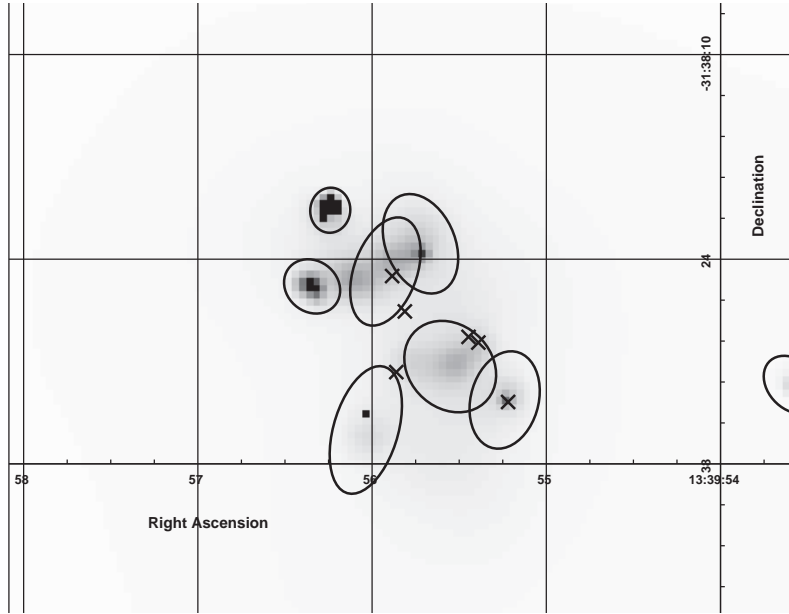


Figure 13. Positions of the six largest optical star clusters are shown as crosses and these are overlaid on the *Chandra* soft-band (0.3–1.1 keV) smoothed X-ray images of NGC 5253. Also overlaid on these images are the X-ray sources detected in the central region of the *Chandra* data, which are labelled in Fig. 12. N is to the top and E to the left and the image is a linear greyscale. The flux densities range from 0 to $7.0 \times 10^{-11} \text{ erg s}^{-1} \text{ cm}^{-2} \text{ arcmin}^{-2}$.

ing that the path length is $\sim 1 \text{ kpc}$ (i.e. comparable to the beam width) leads to $n_0 = 1 \text{ cm}^{-3}$. We note that Martin (1997) inferred densities of $\sim 250 \text{ cm}^{-3}$ in the warm photoionised gas in the core of NGC 5253, though with a filling factor of a percent or so, and that much higher densities are also implied for the smaller volumes associated with the HII regions in NGC 5253 (Turner et al. 1998).

Using these figures in equations 1 and 2 give values for R_B and v_B of 570 pc and 67 km s^{-1} . The size estimate is comparable to the size of the region occupied by the bulk of the X-ray and $\text{H}\alpha$ emitting gases, but no allowance has been made for the effect of the interaction of outflows from the multiple star-clusters present in the central region, while the theory is applicable to the growth of a single bubble. This size estimate is smaller than the size of the reported large-scale $\text{H}\alpha$ shells, their expansion velocities were measured to be $\sim 35 \text{ km s}^{-1}$, which is of roughly the same order as predicted here. It is possible that we may be observing the escape of some stellar wind material through ruptures in the original bubble that are then proceeding to sweep-up and shock more of the ISM lying outside the central region. The emission from such gas has to be at a very low intensity though as it is not detected by either *Chandra* or *XMM-Newton*. The average count rate in the annuli beyond the 0.53 kpc to which the X-ray emission can be traced is $0.05 \pm 0.28 \times 10^{-3} \text{ cts s}^{-1}$, which corresponds to a flux of $\sim 0.3 \pm 1.9 \times 10^{-15} \text{ erg s}^{-1} \text{ cm}^{-2}$. Alternatively, a clumpy environment could allow preferential escape along channels between molecular clouds, although there does not appear to be evidence for the existence of such objects, and the low expansion velocities observed would argue against such uninhabited outflow. There are however two ‘dark clouds’ reported in the West of the galaxy by Hunter (1982).

The superbubble model allows prediction of the X-ray luminosity of an expanding bubble to be made. From Ta-

ble 7, it can be seen that the radiative cooling time for both components of the X-ray emitting gas is long compared to our assumed expansion time of 5 Myr, and so radiative losses can be assumed to be small. Assuming spherical symmetry for the expansion, uniform density for the ambient ISM and a constant rate of kinetic energy injection, the X-ray luminosity is given by

$$L_X = \int n(r)^2 \Lambda_X(T, Z) dV \quad (3)$$

where $\Lambda_X(T, Z)$ is the volume emissivity of the gas being considered. Based on the density $n(r)$ and temperature $T(r)$ profiles (Chu & Mac Low 1990), this equation can be evaluated to yield the X-ray luminosity of the superbubble. Assuming an emissivity of the X-ray emitting gas of $\Lambda = 6.8 \times 10^{-24} \text{ erg s}^{-1} \text{ cm}^3$ (cf Table 7), we find that for NGC 5253

$$L_X = 9.3 \times 10^{36} L_{\text{mech}, 40}^{33/35} n_0^{17/35} t_6^{19/35} \text{ erg s}^{-1}, \quad (4)$$

As discussed earlier, assuming an energy injection rate from the starburst in NGC 5253 of $L_{\text{mech}} = 3.6 \times 10^{40} \text{ erg s}^{-1}$, an ambient density of $n_0 = 1 \text{ cm}^{-3}$ and an age of 5 Myr, leads to a predicted thermal X-ray luminosity for NGC 5253 of $L_X = 0.7 \times 10^{38} \text{ erg s}^{-1}$, which is lower than that observed for the two thermal components ($L_x \sim 4 \times 10^{38} \text{ erg s}^{-1}$, but given the uncertainties in the some of the assumed parameters, and indeed the validity of treating the situation in NGC 5253 as a single superbubble, this is perhaps reasonable agreement).

We note that an estimate of the mechanical energy injection rate can also be obtained from the thermal energy contained within the diffuse X-ray emission. Averaging the values obtained from the *Chandra* and *XMM-Newton* data, the total thermal energy is $3.4 \times 10^{54} \text{ erg}$. Assuming this is the result of complete thermalization of the stellar winds

for the duration of the current starburst, then L_{mech} is $\sim 2.2 \times 10^{40} \text{ erg s}^{-1}$, which is again in broad agreement with that from theoretical considerations of the starburst stellar population.

The total mass of material contained in the X-ray emitting gas obtained from the average figures of the two data sets is $\sim 1.4 \times 10^6 \text{ M}_\odot$ (ignoring the filling factor). If this mass has been injected during the lifetime of the starburst then the mass injection rate is on average $\sim 0.3 \text{ M}_\odot \text{ yr}^{-1}$.

Another estimate of the mass injection rate can be obtained from the fact that for an adiabatic superbubble, the X-ray temperature $T_X \sim 5/11T_0$, where

$$T_0 = \frac{2}{3} \left(\frac{L_{\text{mech}}}{M} \right) \frac{\mu m_H}{k} \text{ K} \quad (5)$$

(Heckman et al. 1995) and is the temperature attained if all the mechanical energy injected by the starburst remains entirely within the shocked wind region. The weighted average temperature of the diffuse X-ray emitting gas (Table 7) is $\sim 5 \times 10^6 \text{ K}$, which gives a value for $T_0 \sim 1.1 \times 10^7 \text{ K}$ and from the assumed L_{mech} , a mass injection rate of $\dot{M} \sim 0.25 \text{ M}_\odot \text{ yr}^{-1}$. Finally, an estimate of the deposited mass from both the stellar winds and conductive evaporation of the swept-up ISM material can be made from the density of the diffuse X-ray emitting gas. This figure depends on the filling factor of the bubble interior but assuming $f = 1$ results in an upper limit. Further, it is necessary to assume that any volume occupied by the swept-up cool shell of ISM and the freely expanding stellar winds is small in comparison to the shocked wind region. With the combined density of the soft and medium components, $n \sim 0.1 \text{ cm}^{-3}$, $V = 1.54 \times 10^{64} \text{ cm}^3$ and all other symbols having their usual meanings,

$$M = \rho V = n \mu m_H \frac{4}{3} \pi R^3 \sim 8 \times 10^5 \text{ M}_\odot, \quad (6)$$

which implies a mass injection rate of $0.16 \text{ M}_\odot \text{ yr}^{-1}$ over 5 Myr.

The mass injection rates into the hot phase derived here from the X-ray observations are thus either slightly above or broadly comparable to the current star-formation rate ($0.2 \text{ M}_\odot \text{ yr}^{-1}$) derived from infrared and H α luminosities (Table 1), but rather higher than the current stellar mass-injection rates.

The mass deposition rate into the hot-phase seen here suggests that if the outflow from the starburst region develops into a superwind and escapes the gravitational potential well of the galaxy then there is substantial scope for both metal-enrichment of, and deposition of large amounts of mass and energy into the IGM. The likelihood of blow-out occurring can be assessed by applying the criterion for blow-out, defined by Mac Low & McCray (1988) to NGC 5253. This defines a parameter Λ , the dimensionless rate of kinetic energy injection, and predicts blow-out if $\Lambda \geq 100$, with Λ given by

$$\Lambda = 10^3 L_{\text{mech},40} H_{\text{kpc}}^{-2} P_4^{-3/2} n_0^{1/2} \quad (7)$$

where $L_{\text{mech},40}$ is the mechanical energy luminosity in units of $10^{40} \text{ erg s}^{-1}$, H_{kpc} is the galaxy scale-height in kpc, and P_4 is the initial pressure of the ISM in units of $P/k = 10^4 \text{ K cm}^{-3}$. For $\Lambda \geq 100$, with $L_{\text{mech},40} = 3.6$, $n_0 = 5 \text{ cm}^{-3}$ and assuming $P_4 \sim 1$ (typical of the value in the Milky

Way), then $H_{\text{kpc}} \leq 9$. The HI halo of NGC 5253 extends to around twice the optical extent $\sim 2'$ ($\sim 1.83 \text{ kpc}$) along the minor axis of the galaxy (Kobulnicky & Skillman 1995). It seems extremely likely then that the hot, metal-enriched gas generated by the current starburst along with the swept-up and conductively evaporated ISM material can escape the gravitational potential well of NGC 5253.

5 SUMMARY AND CONCLUSIONS

In summary, we have presented an X-ray analysis of the important dwarf elliptical, starburst galaxy NGC 5253 using data from both the *Chandra* and *XMM-Newton* satellites. We detected X-ray emission from 31 discrete point sources in the *Chandra* ACIS-S3 chip data with 17 of these lying within the optical extent of the galaxy, as measured by the D_{25} ellipse. Some of these can be clearly identified as X-ray binaries while others seem to be associated with the emission from super star-clusters rather than individual point sources, as they are extended compared to the *Chandra* PSF. The 5 sources in this category (sources 16–20) all lie in the central region of the galaxy and are associated (particularly in the case of sources 17, 18 and 19) with the most intense regions of emission seen on the H α image. The unabsorbed luminosities of these sources in the 0.3–8.0 keV energy band from $(0.25 - 1.50) \times 10^{38} \text{ erg s}^{-1}$.

The majority of the X-ray emission is confined to the central region of the galaxy where the intense, current burst of star-formation is occurring. The extent of the emission also correlates well with that of the H α emission and both are confined to a region of diameter $\sim 1 \text{ kpc}$ in the centre of the galaxy. Both of these emissions are embedded within a spherical distribution of HI that extends out to $\sim 2 \text{ kpc}$ from the centre.

The diffuse X-ray emission in NGC 5253 requires two thermal and one power-law component to best fit its spectrum, suggesting that the hot gas is a multi-phase environment with unresolved point sources, probably lower luminosity X-ray binaries, embedded in it. The fitted gas temperatures are $0.24 \pm 0.01 \text{ keV}$ and $0.75 \pm 0.05 \text{ keV}$ for the soft and medium components respectively and their respective absorption corrected luminosities in the 0.37–6.0 keV band are $(2.19 \pm 0.16) \times 10^{38} \text{ erg s}^{-1}$ and $(1.75 \pm 0.15) \times 10^{38} \text{ erg s}^{-1}$. This emission is seen to be extended in several directions in the *Chandra* data but this is not confirmed by the *XMM-Newton* data. However, the extent is not as great as the $\sim 1 \text{ kpc}$ shells reported to the NW and WSW by Marlowe et al. (1995), in the H α emission. These shells are expanding with velocities of $\sim 35 \text{ km s}^{-1}$ and hence have required $\sim 10 \text{ Myr}$ to have evolved. NGC 5253 is proving to be a rather enigmatic object though, as our analysis of the dynamics of the hot gas are not consistent with the expansion velocity and age of these H α shells.

The hot X-ray emitting gas has a total thermal energy content of $3.4 \times 10^{54} \text{ erg}$ and a total mass of $1.4 \times 10^6 \text{ M}_\odot$. From values in the literature, we assume an age for the starburst responsible for this hot gas of 5 Myr and a value for the density of the ambient ISM of $n_0 = 5 \text{ cm}^{-3}$. The radius of the region in which most of the diffuse X-ray and H α emission is confined is 0.53 kpc. Application of standard superbubble models to NGC 5253's starburst, assum-

ing the age and density above, result in a predicted radius and expansion velocity for a single superbubble of ~ 400 pc and $\sim 50 \text{ km s}^{-1}$, figures which are comparable to those observed.

The main problem here would seem to lie in the fact that no clear bipolar outflow is observed in NGC 5253 and no allowance has been made for the presence of multiple superbubbles in the central region. If the central starburst is young, the bubbles blown around individual star clusters will overlap and impede each others expansion confining the emission to a smaller region than expected and reducing the observed expansion rate. The $\text{H}\alpha$ shells, reported by Marlowe et al. (1995), to the West could be the result of the superbubbles closest to the edge of the central region being able to expand more freely. The lower velocity seen could result from less stars contributing to the energy input in these regions and/or the outflow having experienced some recent deceleration on encountering higher density material such as the dark clouds reported in the West of the galaxy (Hunter 1982). However, our radial surface brightness profile does not show any detectable X-ray emission beyond ~ 0.5 kpc.

NGC 5253 is a very complex object, which shows that standard superbubble models are difficult to apply to dwarf starbursts galaxies. However, the energy injection rate into the galaxy would seem sufficient to allow the expanding hot gas to escape the gravitational potential well of NGC 5253 and its relatively small (~ 1.8 kpc along the minor axis) HI halo would also offer little resistance to this. Thus, it seems likely then that NGC 5253 will lose metal-enriched material, mass and energy as a result of its current bout of star-formation.

ACKNOWLEDGEMENTS

The referee is thanked for a helpful report. LKS and IRS acknowledge funding from a PPARC studentship and Advanced Fellowship respectively. DKS is supported by NASA through *Chandra* Postdoctoral Fellowship Award Number PF0-10012, issued by the *Chandra* X-ray Observatory Center, which is operated by the Smithsonian Astrophysical Observatory for and on behalf of NASA under contract NAS8-39073. Our thanks go to Christy A. Tremonti for kindly providing us with the $\text{H}\alpha$ image of NGC 5253.

REFERENCES

Ardeberg A., de Groot M., 1973, *A&A*, 28, 295

Beck S.C., Turner J.L., Ho P.T.P., Lacy J.H., Kelly D.M., 1996, *ApJ*, 457, 610

Caldwell N., Phillips M.M., 1989, *ApJ*, 338, 789

Calzetti D., Meurer G.R., Bohlin R.C., Garnett D.R., Kinney A.L., Leitherer C., Storchi-Bergmann T., 1997, *AJ*, 114, 1834

Campana S., Moretti A., Lazzati D., Tagliaferri G., 2001, *ApJ*, 560, L65

Castor J., McCray R., Weaver R., 1975, *ApJ*, 200, L107

Chu Y.-H., Mac Low M.-M., 1990, *ApJ*, 365, 510

Colbert E.J.M., Heckman T.M., Ptak A.F., Strickland D.K., 2004, *ApJ*, 602, 231

de Vaucouleurs G. de Vaucouleurs A., Corwin J.R., Buta R.J., Paturel G., Fouque P., 1991, *Third Reference Catalogue of Bright Galaxies, Version 3.9*, University of Texas Press, Austin

Fabbiano G., Kim D-W., Trinchieri G., 1992, *ApJS*, 80, 531

Ferrarese L., et al., 2000, *ApJS*, 128, 431

Freedman W.L., 2001, *ApJ*, 553, 47

González-Delgado R. M., Leitherer C., Heckman T., Cervino M., 1997, *ApJ*, 483, 705

Gorjian V., Turner J.L., Beck S.C., 2001, *ApJ*, 554, L29

Hartwell J.M., Stevens I.R., Strickland D.K., Heckman T.M., Summers L.K., 2003, *MNRAS*, in press

Heckman T.M., Dahlem M., Lehnert M.D., Fabbiano G., Gilmore D., Waller W.H., 1995, *ApJ*, 448, 98

Hunter D.A., 1982, *ApJ*, 260, 81

Hunter D.A., O'Connell R.W., Gallagher J.S., Smecker-Hane T.A., 2000, *AJ*, 120, 2383

Israel F.P., De Bruyn A.G., 1988, *A&A*, 198, 109

Kennicutt Jr. R.C., 1998, *ARA&A*, 36, 189

Kobulnicky H.A., Skillman E.D., 1995, *ApJ*, 454, L121

Legrand F., Kunth D., Mas-Hesse J.M., Lequeux J., 1997, *A&A*, 326, 929

Leitherer C., Heckman T.M., 1995, *ApJS*, 96, 9

Leitherer C., Schaerer D., Goldader J.D., González-Delgado R.M., Robert C., Kune D.F., 1999, *ApJS*, 123, 3

Mac Low M.-M., McCray R., 1988, *ApJ*, 324, 776

Marlowe A.T., Heckman T.M., Wyse R.F.G., Schommer R., 1995, *ApJ*, 438, 563

Marlowe A.T., Meurer G.R., Heckman T.M., Schommer R., 1997, *ApJS*, 112, 285

Marlowe A.T., Meurer G.R., Heckman T.M., 1999, *ApJ*, 522, 183

Martin C.L., Kennicutt Jr. R.C., 1995, *ApJ*, 447, 171

Martin C.L., 1997, *ApJ*, 491, 561

Martin C.L., 1998, *ApJ*, 506, 222

Martin C.L., Kobulnicky H.A., Heckman T.M., 2002, *ApJ*, 574, 663

Meier D.S., Turner J.L., Beck S.C., 2002, *AJ*, 124, 877

Mohan N.R., Anantharamaiah K.R., Goss W.M., 2001, *ApJ*, 557, 659

Ott J., Martin C.L., Walter F., 2003, *ApJ*, 594, 776

Reif K., Mebold U., Goss W. M., van Woerden H., Siegman B., 1982, *A&AS*, 50, 451

Rieke G.H., Lebofsky M.J., Walker C.E., 1988, *ApJ*, 325, 679

Sanders D.B., Mirabel I.F., 1996, *ARA&A*, 34, 749

Schaerer D., Contini T., Kunth D., Meynet G., 1997, *ApJ*, 481, L75

Stevens I.R., Strickland D.K., 1998, *MNRAS*, 294, 523

Strickland D.K., Heckman T.M., Weaver K. A., Dahlem M., 2000, *AJ*, 120, 2695

Strickland D.K., Stevens I.R., 1999, *MNRAS*, 306, 43

Strickland D.K., Stevens I.R., 2000, *MNRAS*, 314, 511

Strickland D.K., Heckman T.M., Weaver K. A., Hoopes C.G., Dahlem M., 2002, *ApJ*, 568, 689

Summers L.K., Stevens I.R., Strickland D.K., Heckman T.M., 2003, *MNRAS*, 342, 690

Tremonti C.A., Calzetti D., Leitherer C., Heckman T.M., 2001, *ApJ*, 555, 322

Turner J.L., Beck S.C., Hurt R.L., 1997, 474, L11

Turner J.L., Ho P.T.P., Beck S.C., 1998, *AJ*, 116, 1212

Turner J.L., Beck S.C., Crosthwaite L.P., Larkin J.E., McLean I.S., Meier D.S., 2003, *Nature*, 423, 621

Walsh J.R., Roy J.-R., 1987, *ApJ*, 319, L57

Weaver K.A., 2001, in *The Central kpc of Starbursts and AGN: The La Palma Connection. ASP Conference Proceedings*, Vol 249, 389, Eds. J.H. Knapen, J.E. Beckman, I. Shlosman, T.J. Mahoney, San Francisco, ASP

Weaver R., McCray R., Castor J., Shapiro P., Moore R., 1977, *ApJ*, 218, 377

Webster B.L., Smith M.G., 1983, *MNRAS*, 204, 743

Zezas A., Fabbiano G., Prestwich A., Ward M., Murray S., 2001, in *The Central kpc of Starbursts and AGN: The La Palma Connection. ASP Conference Proceedings*, Vol 249, 389, Eds.

J.H. Knapen, J.E. Beckman, I. Shlosman, T.J. Mahoney, San
Francisco, ASP